Measuring the Non-Linear Hydrodynamic Response of Higher Flow Harmonics in Pb–Pb at $\sqrt{s_{NN}} = 2.76\,\mathrm{TeV}$

Jasper Parkkila

Master's Thesis
28 June 2017

UNIVERSITY OF JYVÄSKYLÄ
Department of Physics

Supervisor: Dong Jo Kim

Abstract

In ultrarelativistic heavy-ion physics, one of the greatest remaining questions is the interaction properties of the quark-gluon plasma (QGP), i.e. nuclear matter at extreme temperatures. The dynamics of the QGP have been modeled by relativistic hydrodynamics to an impressive level of success. Despite this the free parameter in the theory, the shear viscosity to entropy ratio, is yet to be accurately constrained. By the combined application of carefully constructed initial conditions and the hydrodynamical theory, one may constrain the viscosity to further understand the evolution of the strongly interacting medium.

Traditionally, the constraints for the free parameter are given by a linear relation of the theoretical initial state eccentricities to the experimentally obtainable final state anisotropies. However, due to the large initial state uncertainty, such analysis based on linear relations has been insufficient. Recently, the relation between the higher order anisotropies has been shown to be non-linear. By decomposing the response into linear and non-linear contributions, one obtains a series of coefficients insensitive to the initial conditions and their fluctuations, enabling one to reduce the uncertainties or at least tighten the constraints to theoretical models. In this thesis I shall present the measurement of these coefficients in Pb–Pb at $\sqrt{s_{NN}} = 2.76\,\mathrm{TeV}$ from LHC/ALICE data. The results are compared to theoretical predictions from various publications.

Tiivistelmä

Ultrarelativistisissa raskasionitörmäyksissä syntyvän kvarkki-gluoniplasman (QGP) dynamiikkaa on relativistisella hydrodynamiikalla kuvattu erittäin vakuuttavasti. Teorian vapaa parametri, keskimääräinen viskositeetti-entropiasuhde, on kuitenkin vielä tarkasti määrittämättä. Alustamalla törmäyksen alkutila teoreettisesti sekä soveltamalla relativistista hydrodynamiikkaa QGP:n evoluution mallintamiseen, saadaan viskositeettia tarkastelemalla käsitys QGP:n rakennesosien välisten vuorovaikutusten vahvuuksista, minkä lisäksi voidaan ymmärtää plasman evoluutioon vaikuttavia tekijöitä.

Tavanomaisesti QGP:n viskositeetti määritetään vertailemalla teoreettisen alkutilan eksentrisyyden lineaarista suhdetta kokeellisesti saatavan lopputilan anisotrooppisuuteen. Alkutilan tuoman teoreettisen virheen takia tämä lineaarisiin suhteisiin perustuva analyysi on kuitenkin ollut riittämätöntä. Uusien tutkimusten mukaan vaste korkeammissa kertaluokissa on epälineaarinen. Muodostamalla lineaarisen sekä epälineaarisen vasteen hajotelma saadaan sarja alkutilasta ja sen fluktuaatioista riippumattomia kertoimia, joilla alkutilan epävarmuutta voidaan poistaa. Tässä työssä esitän kertoimien mittaukset LHC/ALICE Pb–Pb $\sqrt{s_{NN}} = 2{,}76\,\text{TeV}$ datasta. Mittauksia vertaillaan teoreettisiin tuloksiin useista eri julkaisuista.

Contents

1 Introduction

1.1 Quark-Gluon Plasma

Background

A form of nuclear matter, where the elementary constituent quarks and gluons are no longer confined into hadronic states, is known as the quark-gluon plasma (QGP). In laboratory conditions its production relies on particle accelerators: at a sufficiently large energy, the accelerated ions are collided with each other, after which the thermal energy resulting from the collision is adequately high to transform the nuclear matter briefly into a plasma state. Once the system has cooled down, the final state of the collision is then observed by a detector as a hadronized particle spectrum, and the properties of this spectrum are then used as the only available experimental probe for the behaviour of the nuclear matter at extreme temperatures.

The experimental study of QGP, from the first attempts at existential evidence to the detailed examination of its material properties, has been an active area of research ever since the first heavy-ion capable accelerators started their operation at Lawrence Berkeley National Laboratory (BEVALAC) [1] and the Joint Institute for Nuclear Research in Dubna [2], accelerating ions up to energies of 1 GeV/nucleon pair. Followed by these pioneering experiments, more progress was made when the Super Proton Synchrotron (SPS) at CERN and the Alternating Gradient Synchrotron (AGS) at BNL, Brookhaven were deployed almost simultaneously in 1986, providing center-of-mass energies of 18 and 5 GeV/nucleon pair [3], respectively. Due to low accelerator energies, none of the experiments could bring any clear evidence about the existence of QGP.

Later in 1994 the first indication of the QGP phase was found, when the SPS was brought to be capable of accelerating heavier lead (Pb) ions at 17 GeV/nucleon pair. Especially the year 2000 was marked by significant developments, during which the first "compelling evidence" of QGP formation from the SPS was reported [4]: the expansion and the anisotropy of the expanded medium. Most notably this was also the year when the Relativistic Heavy Ion Collider (RHIC) was brought online at BNL. The gold ion (Au–Au) beams of RHIC at 200 GeV/nucleon pair further clearly verified the existence of QGP in several experiments, while also allowing probing the behaviour of the said strongly interacting matter [5, 6].

The most powerful accelerator to date remains the Large Hadron Collider (LHC), which in 2010 started its lead ion (Pb–Pb) beams initially at center-of-mass energy 2.76 TeV/nucleon pair. Of the seven LHC experiments the ALICE (A Large Ion Collider Experiment) is the most dedicated to heavy-ion physics and QGP research. The 2010 2.76 TeV data from the ALICE detector is also used for the research of this thesis. Since 2015, collision data in 5.02 TeV energies has also been available. At higher energies the QGP state is expected to live for longer.

Research

One of the major questions is related to the strength and patterns of the interaction in QGP, i.e. how the constituents interact by scattering depending on the general condi-

tions of the matter. Experimental research can only provide information about the final state of the collisions. For this reason to study the QGP itself, modern research relies on theoretical model calculations, in addition to the experimental probing of the collision events. Generally, the research is conducted by comparing the final states, the momentum distribution of the observed particle spectrum or "response", between the heavy-ion collisions from real world experiments and theoretical model calculations, while also taking the theoretically obtained initial state into account [7, 8].

Simulations of the collision events model the evolution of the QGP from the initial state to the final state. The evolution in the model calculations is driven by a parameter describing the interaction strengths of the QGP [9]. If the final states between the experimentally observed collisions and model calculations correspond to each other, further assuming that the initial state was also correctly modeled, it should be reasonable to expect the magnitude of the empirically constrained interaction parameter to better help understand the actual physics behind the QGP. Because of this, a considerable effort in QGP research is put in favor of constraining this parameter.

However, currently the required knowledge of the initial state is incomplete. The uncertainty between the various initial state models is too large, rendering the current methods based on parametric relations to the final state insufficient [10, 11]. This initial state problem will be one of the motivational factors of this thesis, where I introduce one of the recently proposed solutions to this issue, the non-linear response formalism [12–14]. Although an adequately comprehensive introduction will be given, the main purpose of this thesis is not to only review the details of the formalism, but to present the measurements of the related observables, expected to significantly improve the current constraints on the model interaction parameters.

In this thesis I begin by explaining the required background to our analysis. Assuming some basic knowledge on general nuclear structure, I shall first give a short introduction to experimental heavy-ion physics, while also explaining basic concepts of the necessary experimental observables such as the collective flow. I shall also present a brief overview of the crucial theoretical QGP evolution models, namely the fundamentals of relativistic hydrodynamics and parton transport modeling. After this, a more formal definition of the flow and methods to analyze it will follow. This is where I also explain the mechanism of non-linear formalism and its related new observables. I will finally then present the experimental setup and the analysis results and explain some observations.

1.2 Ultrarelativistic Heavy-Ion Physics

Heavy-Ion Collisions

As for the common ordinary substances, the state of the nuclear matter can be visualized with a phase diagram. For this, one employs the equation of state, which couples the different hypothetical state observables (pressure, temperature etc.) for a complete state description. A schematic QCD (quantum chromodynamics) matter phase diagram is shown in Fig. 1. At low temperatures T and the specific baryonic chemical potential μ, the quarks are confined into hadrons, and the matter is in a state as it typically is found in the universe. As the temperature increases, the confinement of the quarks and

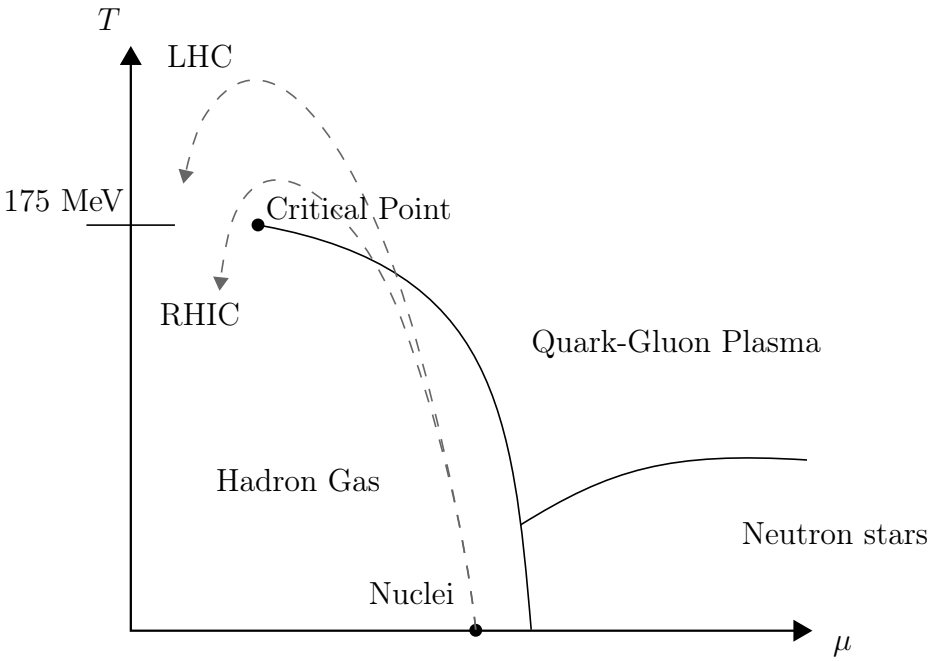

Figure 1: Phase diagram of the QCD, in a typical (μ, T)-representation, where μ is the baryonic chemical potential describing the imbalance between quarks and antiquarks. Based on the QCD lattice calculations [15], the critical point is around $T_c \approx 150 \backsim 175\,\mathrm{MeV}$, approximately $2 \cdot 10^{12}\,\mathrm{K}$. Phase transformation paths that the colliding nuclei might take are sketched for the RHIC and LHC accelerators. After collision, the nuclear matter quickly thermalizes passing the threshold conditions for the QGP state. As the matter expands and eventually cools down, the hadronization begins. During the hadronization process, the QGP and hadronic matter coexist for a brief period of time. The resulting newly created hadrons are decoupled as opposed to the initial single nuclei, also indicated by the significantly lowered chemical potential.

gluons starts to break, and the matter undergoes a phase transition to a plasma state. A theoretical phase diagram and the corresponding equation of state are obtainable with numerical lattice QCD calculations [5], where "lattice" is used to refer to a discretized subsidiary of the QCD continuum gauge theory [16]. In heavy-ion experiments, the goal is to induce the phase transformation to the plasma state, by colliding ions at relativistic energies.

A heavy-ion collision can be modeled as a series of successive phases [17]. A standard description consists of four different stages, as shown in Fig. 2. Immediately after the collision event begins the pre-equilibrium stage (stage 1 in the figure). The time duration of this stage is usually taken to be around 0.2 fm/c or more [18,19]. Stage 2 is the plasma regime, lasting for about 5 to 10 fm/c. This is the thermalization[1] stage dominated by the physics of QGP. Stage 3 is the mixed-phase stage where the temperature has dropped enough for the hadronization to begin and hadronic interactions take place. Once the QGP matter has cooled down, the system is considered to have reached the freeze-out stage (4). The particle production of the event is then shortly after observed by the

[1] A thermal equilibrium is assumed in the model calculations [17].

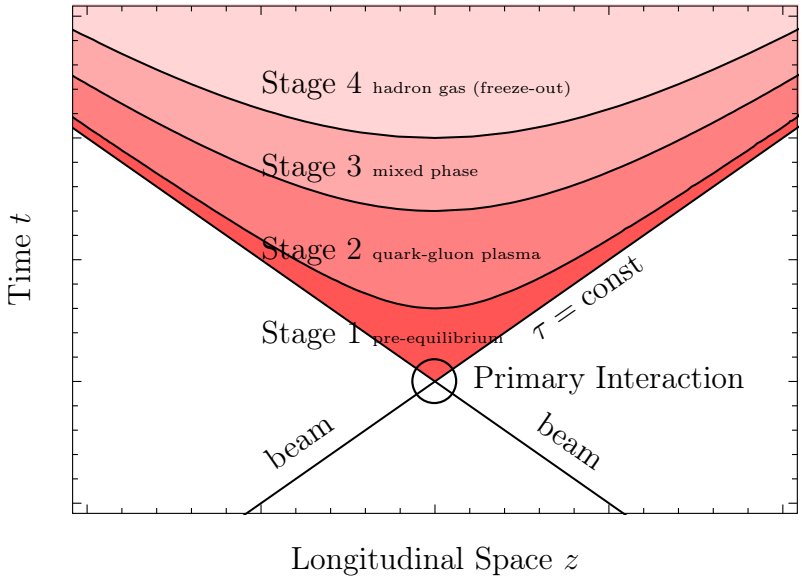

Figure 2: Spacetime evolution of a collision event, showing the division between different stages in an arbitrary (z, t)-representation. The straight lines intersecting at the center portray the colliding nuclei at relativistic speeds. Stages of the collision can be roughly separated by durations of proper time $\tau = \sqrt{t^2 - z^2}$ [17]. Due to the Lorentz-contraction of the detector frame, the collision duration is significantly less than the radius of the nuclei divided by the speed of light. See text for discussion.

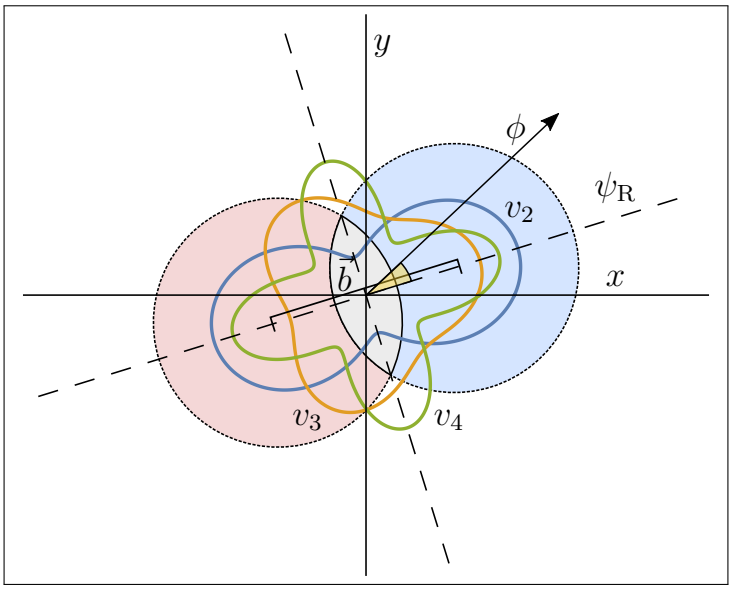

Figure 3: A schematic view of a nuclear collision and the resulting anisotropic flow harmonics ($n \geq 2$), visualized as a polar plot around the participant region (grey). The observed production particle spectrum follows the shape of the initial anisotropy distribution. No symmetry plane fluctuations are considered, i.e. $\psi_n = \psi_{\mathrm{R}} \forall\, n \geq 2$. Coordinate system (x, y) is fixed to the detector's reference frame.

detector. The phase transformations that the matter undergoes is also visualized in the phase diagram in Fig. 1.

A schematic representation of a collision event is presented in Fig. 3. Here two nuclei, separated by the impact parameter $\vec{b}$, undergo a peripheral (non-central) collision. The beam direction defines a reaction plane ψ_{R}, which most of all expresses the symmetry of the collision. The colliding region between the two nuclei is known as the participant region, where the energy density-dependent initial state symmetry is given by the participant planes $\Phi_{m,n}$ of increasing harmonic orders. In a non-central collision, this region has a highly anisotropic almond-like shape. The greater the overlap, the greater the number of participants taking part in the impact. For this reason the number of produced particles is larger in central collisions, which combined with theoretical nuclear models can be utilized in centrality determination [20, 21].

To characterize the initial shape of this system, one defines a set of anisotropy parameters ε_n. The spatial eccentricity, or the coordinate space anisotropy, $\varepsilon_{m,n}$ can be defined as [22]

$$\varepsilon_{m,n}\mathrm{e}^{in\Phi_{m,n}} \equiv -\frac{\langle r^m \mathrm{e}^{in(\varphi-\Phi_{m,n})}\rangle}{\langle r^m\rangle} \equiv -\frac{\int_\Omega \mathrm{d}r\mathrm{d}\varphi r^m \mathrm{e}^{in(\varphi-\Phi_{m,n})}\rho(r,\varphi)}{\int_\Omega \mathrm{d}r\mathrm{d}\varphi r^m \rho(r,\varphi)}, \tag{1}$$

where φ and r are the spatial parameters, $\Phi_{m,n}$ the participant planes and $\rho(r,\varphi)$ is the initial transverse energy density profile. Here a radial weight $m = n$ will be used, and a shorthand notation $\varepsilon_n \equiv \varepsilon_{n,n}$ is to be defined. The eccentricity is obtained from the theoretical initial state models. A change in the second order eccentricity ε_2 expresses an anisotropic, radial pressure gradient driven expansion of the QGP matter. The initial density profile is known to fluctuate event-by-event [23, 24], and due to the symmetry of the system in Fig. 3, the third eccentricity ε_3 "triangularity" is completely induced by these initial state geometry fluctuations. As the system evolves, the spatial eccentricity decreases while the transverse momentum shall increase. Most of the time the initial state at the beginning of QGP stage is considered.

Two theoretical QGP evolution models are used in this thesis, the relativistic hydrodynamics and a multi-phase transport model (AMPT). The hydrodynamic model relies on the conservation laws of fluid dynamics, treating the QGP matter as a near-ideal fluid. One of the required assumptions of hydrodynamics is that the medium is in thermal equilibrium. As such, the hydrodynamics is only applicable to the second stage of the collision process. The AMPT on the other hand includes a parton cascade for the QGP phase. Individual wounded nucleons are converted to partons, which are then scattered from each other. The AMPT also extends the simulation further by including a model for hadronic interactions, although such hadronic models have also been used to extend the hydrodynamic treatment. In both of the models the initial conditions, i.e. the initial density profile, centrality and such are given by a nuclear geometry model. Several different models have been developed [19, 20, 25–27], of which some will be mentioned in later discussion.

These models have shown remarkable success in describing the measured data, and the simulations based on the hydrodynamic and partonic models are a substantial part of QGP heavy-ion physics. Both of these models contain a fundamental parameter for the strength of the QGP constituent interactions. For the hydrodynamic model, this comes as the temperature-dependent shear viscosity to entropy ratio $\eta/s(T)$, while the partonic

model requires the partonic two-body scattering cross section $d\sigma_{gg}/dt$. In this thesis, the said parameter will be mostly referred as the η/s in the hydrodynamics. One of the challenges is to find better ways to constrain these parameters. Some of the experimental observables tend to be more sensitive to altered parameters than the others, while also suffering from larger experimental or theoretical uncertainties.

Anisotropic Response

The final state of a collision event can be observed as a momentum distribution of the particles. This collective, measurable response of the evolution process is known as the flow. Depending on the collision geometry, the magnitude of the flow varies radially indicated by the particle flux into that particular direction. In Fig. 3, a large pressure gradient parallel to the reaction plane has induced an elliptic flow, resulting in (finally) hadronized matter having a momentum distribution also focused in the direction of this anisotropy. Traditionally the flow has been characterized by a set of coefficients v_n, each coming from the Fourier decomposition of the complete flow distribution:

$$\frac{\mathrm{d}N}{\mathrm{d}\phi} \propto \frac{1}{2\pi}(1 + \sum_{n=1}^{\infty} 2v_n \cos(n(\phi - \psi_n)). \tag{2}$$

The term "elliptic" refers to the second order flow harmonic v_2, and is used to describe the collective expansion in nuclear matter. Higher orders such as v_3 "triangular", v_4 "quadrangular" and so on have their own significance in characterizing the response. In Eq. (2), the reaction plane ψ_{R} in Fig. 3 has been generalized to several harmonic dependent symmetry planes ${\psi_n}$[2]. As will be explained next, this is to consider the effects of the initial geometry fluctuations. Historically, any possible initial geometry fluctuations were assumed to be negligible, and as a result some of the older literature may prefer to use the reaction plane ψ_{R} throughout the analysis.

An important aspect of the flow is its relation to the initial density profile, or eccentricity of the colliding nuclei. Firstly, it is believed that the final state anisotropy is directly related to the QGP constituent interaction patterns [29]. A study of the complete final state thus provides a way to examine the collective behaviour in the QGP during the early thermalization stage. One of the key insights is the parametric relation between nuclear eccentricities and the response flow magnitudes. Typically for the second and the third order harmonics, a linear relation $v_n \propto \varepsilon_n$ has been sufficient to describe the response [30] (see Fig. 4). It has also been noted, that a higher shear viscosity reduces the hydrodynamic response to the initial spatial anisotropies [8]. As a result, a ratio v_n/ε_n has been proposed as a constraint for the shear viscosity extraction [31, 32]. Given the initial state of the collision, a theoretical model is employed to simulate the pressure driven evolution of the QGP as soon as it is formed. After the simulated evolution, the resulting momentum space anisotropy can be compared with the experimental results,

[2]The term "event plane" has also been used to describe the symmetry planes. Because of the mixing of various terminology for different concepts and methods, the "event plane" will be reserved for another purpose (namely the symmetry planes reconstructed with the event-plane method explained later), and "symmetry plane" will be used instead.

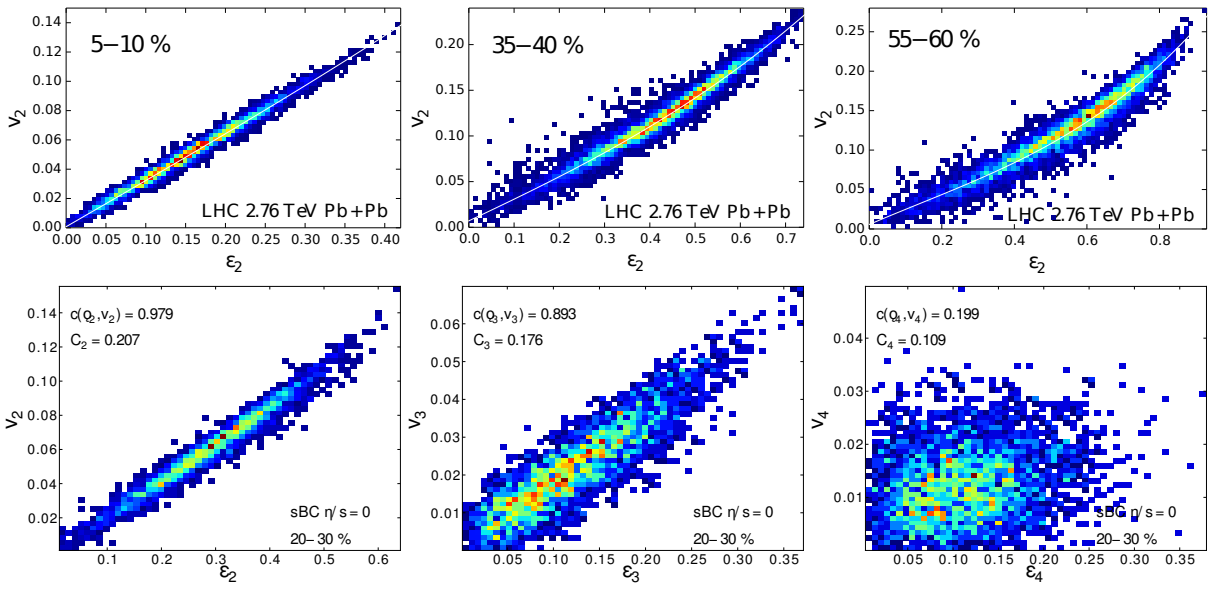

Figure 4: Hydrodynamic $v_n \propto \varepsilon_n$ correlation studies from [19] (above) and [31] (below). For low and mid centrality classes, the relation for $n \leq 3$ is approximately linear.

after normalizing by the eccentricity given by the theoretically modeled initial state. Assuming that the initial state was correctly modeled, and the assumptions regarding the evolution model hold, the average interaction strength can be extracted by simply trying out the best constants and parametrizations.

But as it turns out, there is a non-negligible uncertainty regarding the initial conditions, making the analysis with v_n/ε_n based observables insufficient. In addition to the shear viscosity, the elliptic flow is also sensitive to the initial state fluctuations and the variations between the theoretical models describing them. One solution proposed is to use a combination of elliptic and triangular flow analysis, as the triangular flow removes the large geometry-induced ε_2 eccentricity dependence [8]. It is further expected that because of larger viscous corrections, higher flow harmonics are also increasingly more sensitive to shear viscosity, leading to even better constraints [8]. However, whereas the v_2 and v_3 based observables were mostly limited by the theoretical uncertainties, the higher harmonics are generally more troubled with the experimental precision. This also comes with the fact that the higher order response ($n > 3$) is not linear, as found in the recent studies [12].

Despite initially sounding like an issue, the non-linearity of the higher harmonics can in fact be exploited. In the recently developed non-linear formalism, the non-linear response of the higher $n > 3$ harmonics is decomposed into a linear and non-linear parts [12, 14]. Assuming the linearity holds for the lower harmonics, and the non-correlation of the two contributions, a set of coefficients describing the relative magnitudes of the linear and non-linear responses is obtained. The coefficients representing the ratio between the responses should then intuitively be free of the uncertainty. As opposed to the single v_n based observables, the new coefficients have all the prerequisites to constrain the interaction strength parameters of the evolution models. As always, constraining requires experimental data. This in turn calls for the measurement of these coefficients, which is

the main purpose of this thesis.

Some prior work exists to determine the non-linear coefficients [14]. This work, such as the ATLAS and CMS event-plane measurements [33, 34], also involve studies of correlations between varying flow magnitudes, which can be used to extract the non-linear contributions. In the ATLAS analysis, the non-linearity of the higher orders were investigated based on a different, more complicated method that the one used in our analysis.

The results of this thesis have been produced as a preliminary analysis work for a publication by the ALICE Collaboration. Our analysis has been carried out as follows. From ALICE Pb–Pb $\sqrt{s_{NN}} = 2.76\,\text{TeV}$ data, we compute the required moments which we use for every flow quantity present. We acquire the required event plane observables and study the correlations between coefficients with respect to various directions. Finally, we use this new data to obtain the non-linear coefficients. As part of our analysis we compare our results to simulations, investigate the p_T-dependence and perform various systematic checks to locate sources of potential errors.

2 Theoretical Frameworks

2.1 Hydrodynamic Modeling

Relativistic Hydrodynamics

A successful description of the heavy-ion collisions is given by relativistic hydrodynamics. The application of hydrodynamics in particle physics originates from the early attempts at analyzing collective particle motion as a result of proton-proton collisions [35,36]. Most of all the hydrodynamic model emphasized the importance of a transversely longitudinal, anisotropic expansion of the system rather than an isotropic one expected from an ideal gas [37]. Since the first experimental observations of the QGP matter evolving in a fluid-like manner, the role of the hydrodynamics in heavy-ion physics has been significant. The hydrodynamic treatment has since been refined to model the fluid-like (both ideal and viscous) evolution of the QGP to impressive levels of accuracy.

A general hydrodynamic description relies on the energy and momentum conservation laws of the fluid dynamics. In the case of relativistic hydrodynamics, the local energy-momentum conservation can be expressed by [9, 38]

$$\partial_\mu T^{\mu\nu}(x) = 0, \tag{3}$$

where $T^{\mu\nu}$ is a kinetically defined rank-two energy-momentum tensor and $x = (t, \vec{x})$ a position in spacetime. Note that for a complete fluid description, additional conservation laws may be required, such as the charge conservation in the presence of charged currents. In heavy-ion physics, the charge conservation is governed by the continuity equations for the charged baryon density [9, 38]:

$$\partial_\mu J^\mu_B(x) = 0. \tag{4}$$

Here $J^\mu_B = n_B u^\mu$ is the net baryon current at the given location, a quantity defined by the product of baryon density n_B and its local four-velocity u^μ.

The application of hydrodynamics comes down to a few well-defined assumptions. The first assumption is the local thermal equilibrium, which allows us to decompose Eq. (3) in terms of local energy density and pressure. Omitting the details, one can show [38] that

$$\partial_\mu T^{\mu\nu} = (\epsilon + p + \Pi)u^\mu u^\nu - (p + \Pi)g^{\mu\nu} + \pi^{\mu\nu}, \tag{5}$$

where the energy density ϵ and pressure p quantities are both functions of position. Furthermore, here $g^{\mu\nu}$ is the metric tensor, and Π, $\pi^{\mu\nu}$ are the bulk pressure and shear stress tensor also involving the shear viscosity, respectively.

We may consider a case where Π and $\pi^{\mu\nu}$ are set to vanish. Eq. (5) is then the energy-momentum conservation in case of ideal hydrodynamics, where all the dissipative effects are considered to be negligible. However, generally the fluid behaviour is not ideal, and according to theoretical calculations there is always some small but finite viscosity for all substances [39]. The model calculations have suggested that the QGP behaves as a nearly perfect fluid, with its η/s close to the universal minimum $1/(4\pi) \approx 0.08$ [40]. In

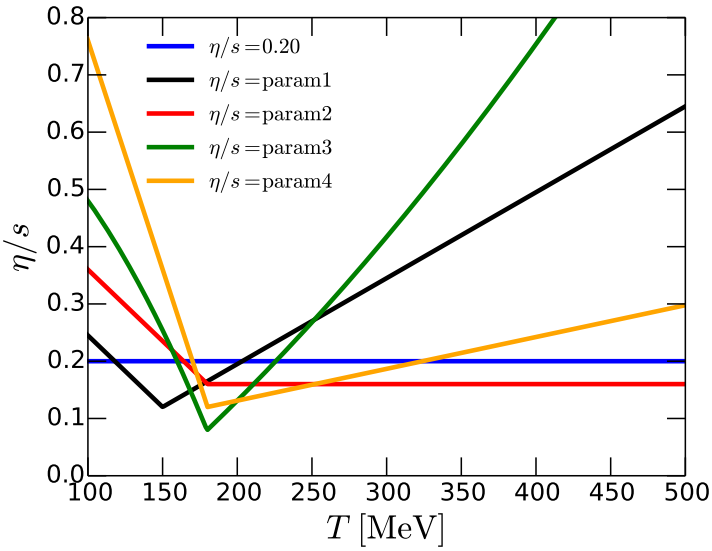

Figure 5: Various parametrizations for the temperature dependence of the shear viscosity to entropy ratio η/s [19]. The minimum is expected to be around the critical point, approximately $T_c \approx 150 \backsim 175\,\mathrm{MeV}$ [15].

some literature, both viscous and non-viscous hydrodynamical models are considered for computational comparisons.

The η/s is known to be temperature dependent. Instead of a constant average value (an average over the full thermalization stage), a temperature dependent parametrization can be applied. Such parametrizations are presented in Fig. 5 [19]. It is worth noting, that as for many other known fluids, the minimal η/s of the QGP can always be found at the vicinity of the critical point [15]. While constraining, finding the minimal temperature for η/s would also verify the location of the said point in the phase diagram.

Like many other theoretical models today, the application of the hydrodynamical model also heavily relies on modern computer simulations. In computational hydrodynamics, the time evolution of the system is obtained by e.g. iteratively time stepping the discretized hydrodynamical equations. For numerical details on relativistic hydrodynamics, the reader is referred to [41].

Equation of State

For the hydrodynamical model to be useful, certain constraints and conditions have to be enforced. Together Eq. (3) – (5) and the possible relations for the bulk density and shear stress define a system of equations. In order to give this system a closed form, the number of equations must equal to the amount of independent variables. This is achieved by involving an additional relation between the state observables, called the equation of state (EoS) of the form

$$p = p(\epsilon, n_B). \tag{6}$$

The purpose of the EoS is to complete the equations by relating the energy density ϵ, pressure p and the baryon density n_B in a thermally equilibratory system. The EoS is

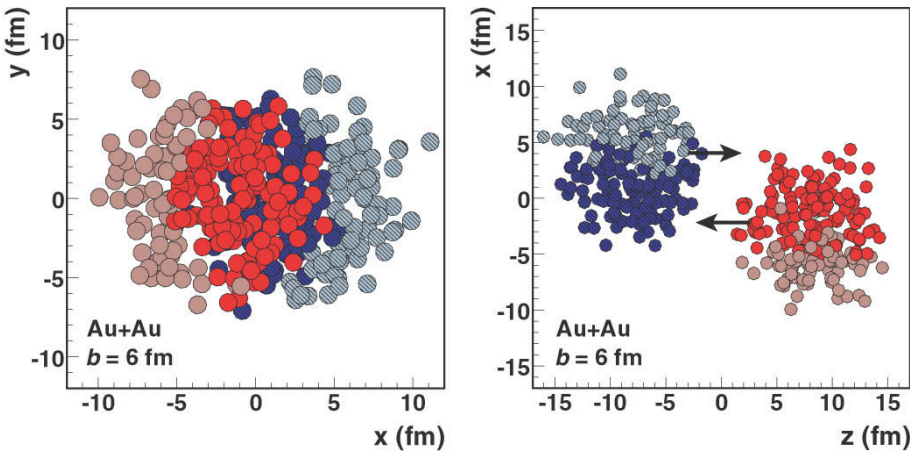

Figure 6: An MC-Glauber event for two colliding gold ions [20]. The participant nucleons in the middle are drawn with more prominent red and blue colors.

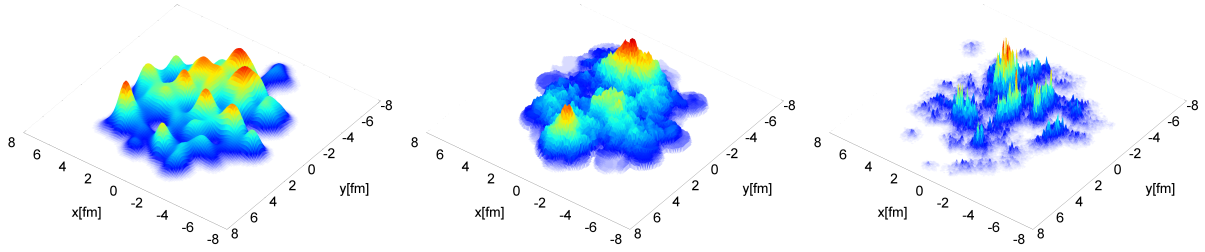

Figure 7: Transverse plane initial density comparison between MC-Glauber, MC-KLN and IP-Glasma (pre-smoothed $\tau \approx 0\,\mathrm{fm/c}$) models [27]. Units of length are mostly arbitrary.

obtainable with lattice QCD simulations [5].

Initial Conditions

Solving a set of differential equations also requires knowledge of the initial state, given in the form of initial conditions. In this case, of particular interest is the state of nuclear matter during the thermalization phase in the heavy-ion collision. Typically a Monte-Carlo based method is used to generate the fluctuating initial conditions. One of such is the Glauber model [20, 25] in which the initial conditions are obtained by randomly sampling nucleons from measured density distributions. A result from such a model is seen in Fig. 6. An initial geometry for the collision is modeled by placing and projecting the two colliding nuclei apart from each other by some randomly chosen impact parameter. Further steps involve computing the interaction probabilities and the calculation of the energy density based on whether the participant nuclei collide or not.

Other extensively studied models include the color-glass-condensate based MC-KLN (Kharzeev-Levin-Nardi) [26, 42] and IP-Glasma [27, 45] for the initial conditions. Compared to the Glauber model, these models differ in the level of detail, and the results vary from smoother energy densities to structurally finer where the color charge fluctuations

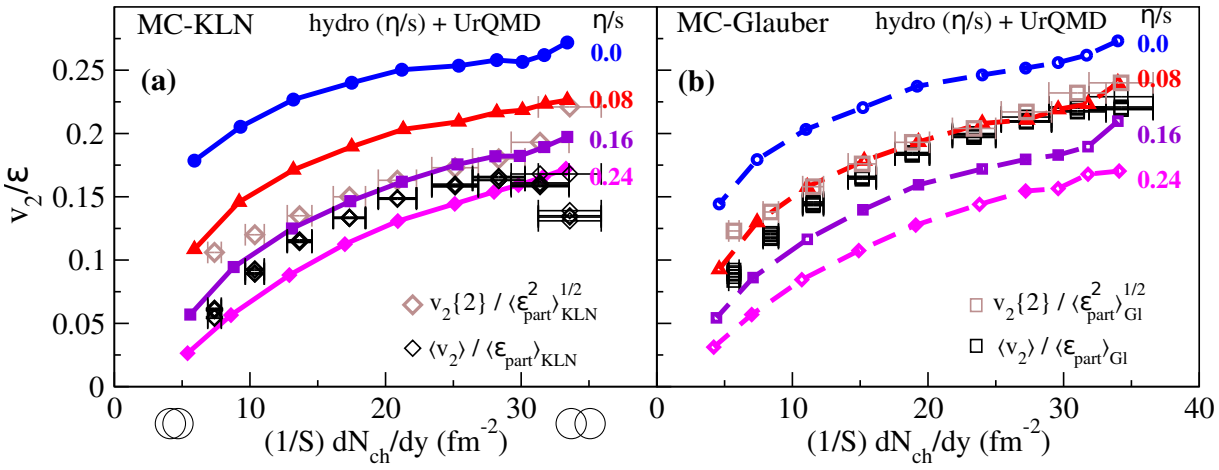

Figure 8: A comparison between theoretical and measured flow results [10], as a function of centrality. On the left, RHIC data with hydrodynamic results using MC-KLN initial conditions is presented. On the right MC-Glauber is used. Results have been scaled using the participant eccentricities given by these two models.

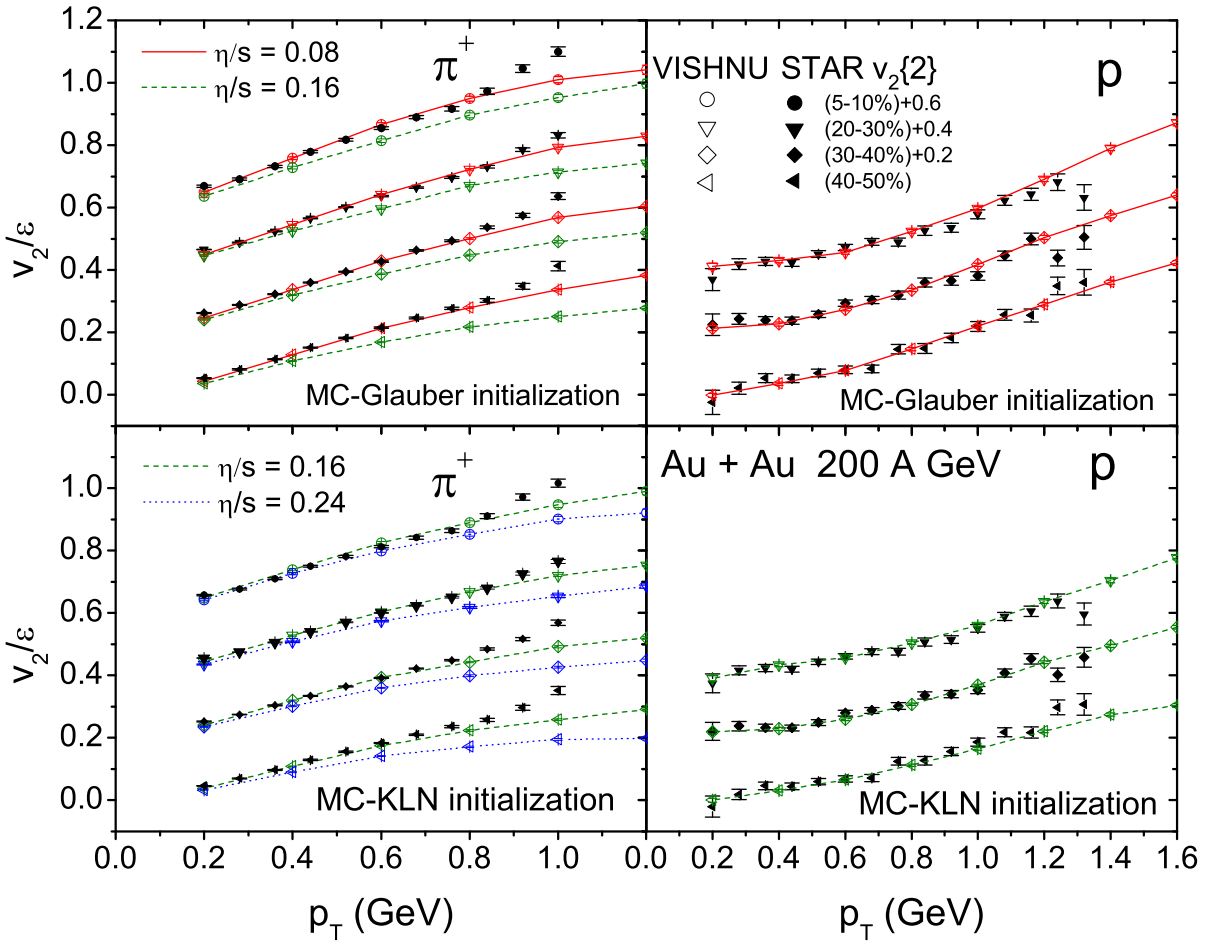

Figure 9: Another set of comparisons for identified pions (left column) and protons (right column) [11] as a function of transverse momentum. Results from the same measurements as in Fig. 8.

have been considered. A comparison between energy densities produced by these models is given in Fig. 7. Of the models shown here, the Glauber produces the smoothest initial conditions. The finest structure is given by the IP-Glasma, although the Yang-Millis evolution also smoothes much of the initial roughness. Compared to the smoother models, this additional granularity also tends to induce larger fluctuation driven odd eccentricities [27, 28, 45].

In Fig. 8, the effect of the different initial conditions on traditional v_n/ε_n observables is emphasized. As a reference data, the study [10, 43] has used the flow from the gold ion collisions measured by the STAR Collaboration [44]. Results from viscous hydrodynamics with four different η/s are presented, and the data is shown as unconnected squares. Between the two initial state models, in both cases the hydrodynamical calculations capture the correct centrality dependence of the observables. However, the initial state uncertainty is clearly visible when normalizing the response by the eccentricities given by these models. Determining the η/s with the Glauber initial conditions gives a slightly smaller result compared to the models with more crude density profiles. Similar observations can be made for Fig. 9 [11], where a comparison has been made for identified particles as a function of transverse momentum. Based on these studies, it was concluded [10, 11] that the resulting η/s varies within the range of 0.08 to 0.24.

Hadronization

To be able to do any comparisons between simulations and real experiments, the hydrodynamically evolved energy density has to be converted into a particle spectrum corresponding to the measured distributions obtained in heavy-ion experiments. Once sufficient evolution stopping conditions have been reached, the particle spectrum is obtained using the Cooper-Fry formula [46]

$$E\frac{dN}{d^3p} = \int_\sigma \mathrm{d}\sigma_\mu p^\mu f, \tag{7}$$

where σ is the surface of condensation and f a particle distribution function of thermodynamical observables. Determination of the final state can be done by thresholding specific observables (such as the freeze-out temperature), although more accurate methods based on comparisons of expansion and scattering rates have also been proposed [47, 48].

2.2 A Multi-Phase Transport Model

Cascade Simulation

An alternative method to QGP-modeling is to regard the collision as a series of partonic interactions. Whereas the hydrodynamic modeling was based on the equations of fluid dynamics, the so-called hadronic and partonic cascade simulations rely much more on Monte-Carlo based simulations to dictate the individual processes between reaction candidates. One collection of such steps for the initialization, interaction modeling and termination is known as the AMPT, a multi-phase transport model.

In a multi-phase transport model the colliding nuclei undergo four different phases [49, 50]. These are the generation of the initial conditions, the partonic interactions, the conversion to hadronic matter and finally the hadronic interactions. The basic idea of the

partonic cascade phase of the AMPT is to simulate parton scattering events according to interaction probabilities given by the cross sections of the pQCD, also directly related to the shear viscosity used in hydrodynamics [50]. In a transport model, the parton interactions are described by the equations of motion for parton density distributions $f_a(\vec{x},\vec{p},t)$ (for type a parton) [49]. These equations may be approximated by the Boltzmann equations

$$\begin{aligned} & p^\mu \partial_\mu f_a(\vec{x},\vec{p}_{b(i)},t) \\ & = \sum_m \sum_{b(1),\ldots,b(m)} \int \prod_{i=1}^{m} \frac{\mathrm{d}^3 p_{b(i)}}{(2\pi)^3 2E_{b(i)}} f_{b(i)}(\vec{x},\vec{p}_{b(i)},t) \\ & \times \sum_n \sum_{c(1),\ldots,c(m)} \int \prod_{j=1}^{n} \frac{\mathrm{d}^3 p_{c(j)}}{(2\pi)^3 2E_{c(j)}} |\mathcal{M}_{m\to n}|^2 \\ & \times (2\pi)^4 \delta^4 \left(\sum_{k=1}^{m} p_{b(k)} - \sum_{l=1}^{n} p_{c(l)} \right) \\ & \times \left[-\sum_{q=1}^{m} \delta_{ab(q)} \delta^3(\vec{p}-\vec{p}_{b(q)}) + \sum_{r=1}^{n} \delta_{ac(r)} \delta^3(\vec{p}-\vec{p}_{c(r)}) \right], \end{aligned} \tag{8}$$

or in the reduced two-body form

$$p^\mu \partial_\mu f(\vec{x},\vec{p},t) \propto \int \sigma_{gg} f(\vec{x}_1,\vec{p}_1,t) f(\vec{x}_2,\vec{p}_2,t) \tag{9}$$

which the partonic cascade model attempts to solve. In Zhang's parton cascade (ZPC) [51], which currently is limited to $gg \to gg$ interactions, two partons scatter whenever they reach the closest interaction distance. The interaction probability is determined by the differential cross section

$$\frac{d\sigma_{gg}}{dt} = \frac{9\pi\alpha_s^2}{2(t-\mu^2)^2}, \tag{10}$$

where t is a basic Mandelstam variable, α_s the strong coupling constant and μ the Debye screening mass in partonic matter. Scattering events are simulated for some specific duration of time, until the scattering is considered to have stopped.

Initial Conditions

Initial conditions for the AMPT are produced with the HIJING (Heavy Ion Jet Interaction Generator) model [52, 53]. These conditions include the soft string excitations (among wounded nucleons, nucleons that underwent a collision) and the spatial and momentum distributions of the produced partons. HIJING employs a binary collision model between the two colliding nuclei. The number of binary collisions is determined by the Glauber geometry, where the nuclear density profiles are assumed to have Wood-Saxon shaped distributions.

For each binary collision HIJING uses the eikonal formalism to evaluate nuclear interaction probabilities for parton jet outputs [53]. After the jet producing hard scattering processes have been modeled, the remaining energy is used for the soft string excitations. The excited string system may then further experience more collisions.

There are two variations of the AMPT model, the original default and the extended string melting version. The main difference between the versions concerns how the remaining excited strings are handled during the initial conditioning stage. In the string melting version, non-projectile and nucleon targeting strings are converted into partons according to the flavor and spin structures of their valence quarks [49]. This additional mechanism attempts to correct the underestimated partonic effect associated with the excited strings in high energy density regions [54]. In the absence of partonic and hadronic interactions, the string melting version reduces to the default one, provided that the parton formation time was correctly selected.

Similarly to the shear viscosity in the hydrodynamic model, one may attempt to constrain corresponding parameters of the AMPT. One may write a relation between the η/s and partonic model transport cross section. Considering the viscosity of the kinetic theory, and the entropy density in terms of quarks and antiquarks, the relation is given in [50] by

$$\frac{\eta}{s} \approx \frac{3\pi}{40\alpha_s^2}\left[\left(9+\frac{\mu^2}{T^2}\right)\ln\left(\frac{18+\mu^2/T^2}{\mu^2/T^2}\right)-18\right]^{-1}. \tag{11}$$

Hadronization

The hadronization process begins already during the partonic cascade. This results in a coexistence of newly produced hadrons and still scattering partons. Since the different versions of the AMPT produce a different set of post-partonic conditions, some differences are also present at the stage of hadronization. In the default version partons are combined with their parent strings, the remainings of the original nuclei. These new excited strings are then hadronized according to the Lund string fragmentation model [55]. In the Lund model strings fragment into quark-antiquark pairs, which are further used to form hadrons according to the model's symmetric fragmentation function.

For the string melting version a quark coalescence model is used to perform the hadronization [49]. Here two nearest partons are combined into a meson, and three nearest (anti)quarks into some (anti)baryon according to the quarks' flavor and invariant mass. In both default and the string melting versions, newly created hadrons are given a short additional formation time, during which they are not yet allowed to scatter with other hadrons.

The AMPT model includes a model for hadronic interactions, ART (a relativistic transport model) [56, 57]. During this hadronic cascade phase the final products of the partonic simulation are allowed to scatter with each other, elastically and inelastically. For interacting species baryon-baryon, baryon-meson and meson-meson pairs are supported. The hadronic interactions stage of the simulation is commonly referred to as "rescattering". To study the effect of the rescattering, results will be provided with rescattering both enabled and disabled.

Configurations

The AMPT model can be run in two main configurations, the default and the string melting version. In both configurations, the dynamics of the subsequent hadronic matter is described by ART. The third version used in this thesis is based on the string melting

Table 1: The AMPT configurations.

Label	String Melting	Rescattering
Default	N/A	On
Str.m	On	On
Str.m w/o Rescattering	On	Off

configuration in which the hadronic rescattering phase is switched off to study its influence. The different configurations for the model comparison are summarized in Table 1.

3 Experimental Relations

3.1 Anisotropic Flow

Definition

A practical and standard way to characterize the anisotropic flow is to decompose its azimuthal distribution in terms of a Fourier series [58,60]. The Fourier series for a periodic function (period $P = \pi$) can be written as

$$f(\phi) = \frac{a_0}{2\pi} + \frac{1}{\pi}(\sum_{n=1}^{\infty} a_n \cos(n\phi) + \sum_{n=1}^{\infty} b_n \sin(n\phi)), \tag{12}$$

where $a_n = \int_{-\pi}^{\pi} f(\phi)\cos(n\phi)\mathrm{d}x$ and $b_n = \int_{-\pi}^{\pi} f(\phi)\sin(n\phi)\mathrm{d}x$. With a finite number of particles, the integrals become sums. To write the series in terms of just one harmonic flow coefficient, one defines

$$v_n = \sqrt{a_n^2 + b_n^2}, \tag{13}$$

so that for Eq. (12) $a_n = v_n \cos(n\psi_n)$ and $b_n = v_n \sin(n\psi_n)$. Substituting these one finally gets

$$\frac{\mathrm{d}N}{\mathrm{d}\phi} \propto \frac{1}{2\pi}(1 + \sum_{n=1}^{\infty} 2v_n \cos(n(\phi - \psi_n))), \tag{14}$$

where the sine-terms have vanished due to ψ_n momentum symmetry: an integral over sines of particle angles (with respect to the symmetry plane) equals to zero in the case of equal probability for inverted $\phi \to -\phi$ emittance directions. An explicit expression for the flow harmonics can be obtained by integrating over the normalized distribution. Using trigonometric orthogonality relations, one can show that

$$v_n = \langle \cos(n(\phi - \psi_n)) \rangle, \tag{15}$$

where the brackets denote an average over all particles in all events, potentially limited to some event centrality class.[3] Eq. (15) gives the definition of collective flow: a correlation between the azimuthal angle ϕ of a particle to a symmetry plane of a non-central heavy-ion collision. Due to low number of emitted particles per event, an average over all events is preferred to reconstruct the underlying probability distribution.

An equivalent and also commonly used notation may be written with exponential complex quantities. With complex quantities, Eq. (12) takes the form

$$\frac{\mathrm{d}N}{\mathrm{d}\phi} \propto \frac{1}{2\pi} \sum_{n=-\infty}^{\infty} \underbrace{\langle \mathrm{e}^{in\phi} \rangle}_{V_n} \mathrm{e}^{-in\phi}, \tag{16}$$

where $V_n \equiv \langle \mathrm{e}^{in\phi} \rangle = v_n \mathrm{e}^{in\psi_n}$ corresponds to the definition in Eq. (15). An uppercase V_n is used to denote a flow quantity, which in addition to its magnitude also includes its

[3] From here on, an implicit centrality class restriction will be assumed for all averages concerning event groups.

direction. Such a quantity will be useful in more complicated analysis such as the one involving mixed harmonic event-plane correlations.

According to the formalism given by Eq. (14), only even harmonics should have a non-zero flow amplitude. This is due to the fact that also the opposite directions $\phi \to \phi+\pi$ have an equal chance of having a particle emitted. In realistic situations however, as a result of event-by-event initial geometry fluctuations, the average flow for the odd harmonics is typically non-zero. Some details about the consequences of the initial fluctuations [59] were given in section 1.2.

Harmonic Projection

It is possible to measure a flow quantity relative to another harmonic direction instead of its own. To get the flow with respect to the direction of the other, one projects the harmonic on to the desired symmetry plane.

Consider a generic projection of a flow vector V_n on to the direction of V_m, analogous to a basic vector projection $a_1 = |\mathbf{a}|\cos(\theta_{ab}) = \mathbf{a}\cdot\mathbf{b}/|\mathbf{b}|$. Additionally, both of the directional angles ψ_n and ψ_m have been scaled by some integer a_n and a_m, respectively:

$$v_n\{\psi_m\}(a_n, a_m) = v_n\{\psi_n\}\langle\cos(a_n\psi_n + a_m\psi_m)\rangle = \frac{\mathrm{Re}\langle V_n^{\frac{a_n}{n}} V_m^{\frac{a_m}{m}}\rangle}{\sqrt{\langle|V_m|^{2\frac{a_m}{m}}\rangle}}. \tag{17}$$

A notation $v_n\{\psi_m\}$ is used to denote a flow coefficient projected onto other direction ψ_m. To retain the harmonic symmetry properties for relative angles between the symmetry planes, two conditions have to be satisfied [33, 61, 62]. Firstly, an l^{th}-order l-folded symmetric harmonic has to be invariant under phase transformations $\psi_l \to \psi_l + 2\pi/l$. This is satisfied when $a_n|n$ and $a_m|m$. The second condition requires the sum of the coefficients to vanish: $a_n + a_m = 0$, i.e. $a_m = -a_n$. Both of the conditions are met when a least common multiple (LCM) between the harmonic integers n and m is chosen for the angle scaling:

$$a_n\psi_n + a_m\psi_m \to k(\psi_n - \psi_m), \tag{18}$$

where $k = \mathrm{LCM}(n, m)$. A symmetrically valid projection can then be written as

$$v_n\{\psi_m\}(k, -k) = v_n\{\psi_n\}\langle\cos(k(\psi_n - \psi_m))\rangle = \frac{\mathrm{Re}\langle V_n^{\frac{k}{n}}(V_m^*)^{\frac{k}{m}}\rangle}{\sqrt{\langle|V_m|^{2\frac{k}{m}}\rangle}}, \tag{19}$$

where a complex conjugate (*) is used to negate the exponent factor.

Eq. (19) is then used to obtain some projections of interest. By projecting the higher harmonics on to the lower ones, one can for example analyze the fourth order flow with respect to the direction of the second one [14]. For the sixth order the directions are those

of second and third:

$$\begin{aligned} v_4\{\psi_2\} &= \frac{\mathrm{Re}\langle V_4(V_2^*)^2\rangle}{\sqrt{\langle|V_2|^4\rangle}} = \frac{\langle v_4 v_2^2\cos(4\psi_4 - 4\psi_2)\rangle}{\sqrt{\langle v_2^4\rangle}}, \\ v_6\{\psi_2\} &= \frac{\mathrm{Re}\langle V_6(V_2^*)^3\rangle}{\sqrt{\langle|V_2|^4\rangle}} = \frac{\langle v_6 v_2^3\cos(6\psi_6 - 6\psi_2)\rangle}{\sqrt{\langle v_2^6\rangle}}, \\ v_6\{\psi_3\} &= \frac{\mathrm{Re}\langle V_6(V_3^*)^2\rangle}{\sqrt{\langle|V_3|^4\rangle}} = \frac{\langle v_6 v_3^2\cos(6\psi_6 - 6\psi_3)\rangle}{\sqrt{\langle v_3^4\rangle}}. \end{aligned} \tag{20}$$

Inserting the definition of V_n, one obtains the real valued counterparts on the right-hand side.

From the required constraints it should be obvious that Eq. (19) can only be used to generate projections of even harmonics, without involving any additional exponent factors. For even harmonics the projection might be generalized to an arbitrary number of symmetry planes:

$$v_n\{\psi_m\}(c_1, c_2, \ldots, c_l) = v_n\{\psi_n\}\langle\cos(\sum_{j=1}^{l} j c_j \psi_j)\rangle = \frac{\mathrm{Re}\langle V_1^{c_1} V_2^{c_2}\ldots V_l^{c_l}\rangle}{\sqrt{\langle|V_1|^{2c_1}|V_2|^{2c_2}\ldots|V_l|^{2c_l}\rangle}}, \tag{21}$$

for which a constraint $c_1 + 2c_2 + \cdots + lc_l = 0$ is enforced [61], also satisfied by the two-plane variation in Eq. (19). Using Eq. (21), projections of odd harmonics on to multiple symmetry planes may be obtained:

$$\begin{aligned} v_5\{\psi_{23}\} &= \frac{\mathrm{Re}\langle V_5 V_2^* V_3^*\rangle}{\sqrt{\langle|V_2|^2|V_3|^2\rangle}} = \frac{\langle v_5 v_2 v_3\cos(5\psi_5 - 2\psi_2 - 3\psi_3)\rangle}{\sqrt{\langle v_2^2 v_3^2\rangle}}, \\ v_7\{\psi_{23}\} &= \frac{\mathrm{Re}\langle V_7(V_2^*)^2 V_3^*\rangle}{\sqrt{\langle|V_2|^4|V_3|^2\rangle}} = \frac{\langle v_7 v_2^2 v_3\cos(7\psi_7 - 4\psi_2 - 3\psi_3)\rangle}{\sqrt{\langle v_2^4 v_3^2\rangle}}. \end{aligned} \tag{22}$$

Equations in (20) and (22) are used to study the correlations between event-planes, measuring the contribution in higher order flow induced by the lower orders. Additionally, the quantities will later be used in defining the non-linear coefficients. More details will be given in sections 4.1 and 4.2.

Analytic Considerations

Although Eq. (15) is valid, its application in realistic heavy-ion experiments is severely limited. One of the major reasons is its reliance on the symmetry plane quantity ψ_n. Unlike in simulations, where this might be given by the Glauber model for example, this quantity cannot be experimentally determined. Furthermore, the symmetry planes are not constant over the collision events, so no common coordinate system between multiple events exist.

An alternative approach is employed for data analysis on experimental data. Among common possible solutions are the event-plane method [60, 66], its derivative scalar-product variation [63, 66] and the multi-particle correlations [67, 68], which are used to reconstruct the flow coefficients without knowledge of the reaction plane. The results of

this thesis rely on the scalar product and multi-particle correlations, so the methods based on these will be briefly explained next.

A common tool for many reconstruction methods is the flow vector [69], which is the vector sum of all particle directions in a single event. Both scalar product and multi-particle methods make extensive use of this quantity. The weighted flow vector, also known as the Q-vector is defined as

$$Q_{n,p} = \sum_{k=1}^{M} \omega_k^p \mathrm{e}^{in\phi_k}, \tag{23}$$

where M is the number of particles in the event, ω an optional contribution weight and p an implementation-related parameter. For ω the particle transverse momentum can be used, which well approximates the ideal weight $v_n(p_T)$. Weighting may improve the results in some cases, although in this study no weighting will be used, i.e. $\omega = 1$.

Non-Flow Contributions

While discussing the methods for the reconstruction, an additional flow contribution known as the non-flow [68, 70], denoted with δ, will also be mentioned. This unwanted contribution from jet correlations, resonance decays and such not originating from the collision anisotropies can be written as

$$\langle Q_A Q_B \rangle = \langle Q_A \rangle \langle Q_B \rangle + \delta \tag{24}$$

in the case of a correlator of two Q-vectors Q_A and Q_B. The non-flow will be considered an experimental uncertainty, and methods to minimize the non-flow contributions will be detailed.

3.2 Scalar Product Method

Event-plane Resolution

The event-plane (EP) and the scalar product (SP) methods are closely related, so it suffices to introduce the concept of the former first. The original idea of the event-plane method was to use the flow vector as an estimate for the true reaction plane [69]. The large statistical error, coming from the low multiplicity, is corrected for by introducing the concept of the event-plane resolution.

From here on, the symmetry planes reconstructed with the event-plane method will be correspondingly called event-planes, to indicate a presence of an approximation. An approximate flow is acquired as in Eq. (15), except that here the true reaction plane ψ_R (or in this case the symmetry plane ψ_n) has been replaced with an estimate:

$$v_n^{\mathrm{obs}} = \langle \cos(n(\phi - \widetilde{\psi}_n)) \rangle, \tag{25}$$

where the estimate $\widetilde{\psi}_n$ is obtained from the Q-vector:

$$\widetilde{\psi}_n = \frac{1}{n} \arctan\left(\frac{\mathrm{Im}(Q_{n,1})}{\mathrm{Re}(Q_{n,1})} \right). \tag{26}$$

The observed v_n^{obs} is then corrected for by dividing it by the event-plane resolution:

$$v_n = \frac{v_n^{\text{obs}}}{\mathcal{R}_n}. \tag{27}$$

The resolution $\mathcal{R}_n$ is defined as the estimate's deviation from the true reaction plane,

$$\mathcal{R}_n = \langle \cos(n(\widetilde{\psi}_n - \psi_n)) \rangle = \frac{\sqrt{\pi}}{2} \chi \mathrm{e}^{-\frac{\chi^2}{2}} \left[I_{\frac{n-1}{n}} \left(\frac{\chi^2}{2} \right) + I_{\frac{n+1}{n}} \left(\frac{\chi^2}{2} \right) \right], \tag{28}$$

where $\chi = v_n \sqrt{M}$ is a resolution parameter [29] for an event of multiplicity M and I the modified Bessel function

$$I_n(z) = \frac{1}{\pi} \int_0^{\pi} \mathrm{e}^{z \cos(\theta)} \cos(n\theta) \mathrm{d}\theta, \quad n \in \mathbb{Z}. \tag{29}$$

Eq. (28) is not used due to the unavailable quantities in the middle part and the implicit form of the right-hand side. Instead, a subevent method based on symmetrically identical reference detectors is employed.

Subevents and Reference Detector

More formally the complete event-plane method can be derived with the help of Q-vectors. By definition the event-plane method correlates a small group of particles of interest ("POI", identified particles, optionally further narrowed by a p_T condition[4], for example) with a much larger group of background particles (unidentified reference detector particles) [66]. A correlation to a reference group is required to fight the larger statistical fluctuation caused by the low event multiplicity. This correlation can be expressed as

$$\left\langle Q_n \frac{Q_{nA}^*}{|Q_{nA}|} \right\rangle = \underbrace{\langle Q_n \mathrm{e}^{-in\psi_n} \rangle}_{v_n} \underbrace{\left\langle \frac{Q_{nA}}{|Q_{nA}|} \mathrm{e}^{-in\psi_n} \right\rangle^*}_{\mathcal{R}_{nA}}, \tag{30}$$

where on the right hand side the correlation has been factorized by the assumption that the particles of interest Q_n and the reference Q_{nA} are uncorrelated, except for the flow direction $\widetilde{\psi}_n$. On the right hand side one can also further identify the factors as the flow coefficient and the reference detector event-plane resolution in terms of Q-vectors. Solving this for v_n a relation to Eq. (27) is obtained.

To estimate the resolution, the subevent method is used. In the subevent method, two or more subsets are taken from the reference particles from the original event. Subevent multiplicities should be equal.[5] The flow vectors of these subevents are then correlated with each other. In its simplest form, two subevents are used. A correlation between these two can be written as

$$\left\langle \frac{Q_{nA}}{|Q_{nA}|} \frac{Q_{nB}^*}{|Q_{nB}|} \right\rangle = \underbrace{\left\langle \frac{Q_{nA}}{|Q_{nA}|} \mathrm{e}^{-in\psi_n} \right\rangle \left\langle \frac{Q_{nB}^*}{|Q_{nB}|} \mathrm{e}^{-in\psi_n} \right\rangle^*}_{\left| \left\langle \frac{Q_{nA}}{|Q_{nA}|} \mathrm{e}^{-in\psi_n} \right\rangle \right|^2 \equiv \mathcal{R}_{nA}^2}, \tag{31}$$

[4]Correlating only selected particles with the reference allows one to obtain the flow as a function of some property, such as the transverse momentum p_T.

[5]Failure to match the subevent distributions will result in raised non-flow contributions, increasing the variance of the results.

where on the right side factorization has been used again. Since the subevent distributions are supposed to be identical, the subevent resolutions can be combined, leaving us a square of the final resolution. Particle selection for the subevents can be done randomly (in a uniform manner), or by pseudorapidity η, separating the subevents around the midrapidity [60] (ie. η-gap) to reduce the non-flow effects [64, 65].

Explicit methods

Combining the results of equations (30) and (31), one finally gets an evaluable form for the two-subevent event-plane method:

$$v_n\{\mathrm{EP}\} \equiv \left\langle Q_n \frac{Q_{nA}^*}{|Q_{nA}|} \right\rangle \Big/ \sqrt{\left\langle \frac{Q_{nA}}{|Q_{nA}|} \frac{Q_{nB}^*}{|Q_{nB}|} \right\rangle}. \tag{32}$$

Typically an "EP" label is used to explicitly denote a coefficient extracted with the event-plane method. By slightly modifying the above result, one can also obtain the scalar product variation. Removing the normalizations by $|Q_{n*}|$ in both numerator and denominator, one gets

$$v_n\{\mathrm{SP}\} \equiv \langle Q_n Q_{nA}^* \rangle / \sqrt{\langle Q_{nA} Q_{nB}^* \rangle}. \tag{33}$$

By "scalar product" one refers to the complex product in the denominator. Derivation is practically identical to the event-plane method. There are advantages of using the scalar product method over the event-plane [66], especially in the presence of flow fluctuations, where the factorizations used in equations (30) and (31) no longer applies.

If no differential analysis is required, the method may be reduced to consider the whole spectrum of particles as POI. In the case of the scalar product method, the resulting coefficient is calculated from just the two subevents:

$$v_n\{\mathrm{SP}\} \equiv \sqrt{\langle Q_{nA} Q_{nB}^* \rangle}. \tag{34}$$

The individual single $v_n\{\psi_n\}$ calculations in this analysis rely on Eq. (34). No differential analysis is performed, rather the selection is restricted to a large, gradually narrowing p_T-cuts where good statistics can be preserved.

When calculating quantities with mixed event-plane angles, the scalar product method needs to be generalized for the harmonic projections of the flow [79]. Using a generic moment of the form

$$\mathcal{M} = \left\langle \prod_n (V_n)^{k_n} (V_n^*)^{l_n} \right\rangle = \left\langle \prod_n (Q_{nA})^{k_n} (Q_{nB}^*)^{l_n} \right\rangle, \tag{35}$$

one generalizes the scalar-product method for subevents of arbitrary harmonics [14, 79]. Using this to the results in (20) and (22), the explicit method becomes

$$v_4\{\psi_2\} = \frac{\mathrm{Re}\langle Q_{4A} (Q_{2B}^*)^2 \rangle}{\sqrt{\mathrm{Re}\langle Q_{2A}^2 (Q_{2B}^*)^2 \rangle}}, \tag{36}$$

with $k_4 = 1$, $l_2 = 2$ and

$$v_5\{\psi_{23}\} = \frac{\mathrm{Re}\langle Q_{5A} Q_{2B}^* Q_{3B}^* \rangle}{\sqrt{\mathrm{Re}\langle Q_{2A} Q_{3A} Q_{2B}^* Q_{3B}^* \rangle}}, \tag{37}$$

with $k_5 = 1$, $l_2 = l_3 = 1$ as an example. The rest of the correlations for non-differential analysis are obtained similarly.

3.3 Multi-Particle Correlations

Two-Particle Correlations

In multi-particle correlations, instead of considering a distribution of single particles, pairs or groups of multiple individuals are examined [68, 71, 77]. Here the emphasis will be put on two-particle correlations. The analysis starts by forming a pair distribution from the product of two single particle distributions (16) [71]. This leads to

$$\langle \mathrm{e}^{in(\phi_a - \phi_b)} \rangle = \langle \mathrm{e}^{in\phi_a} \rangle \langle \mathrm{e}^{-in\phi_b} \rangle = \langle v_n^a v_n^b \underbrace{\mathrm{e}^{in(\psi_{a,n} - \psi_{b,n})}}_{\approx 0} \rangle \tag{38}$$

and

$$\frac{\mathrm{d}N_{\mathrm{pair}}}{\mathrm{d}\Delta\phi} \propto \frac{1}{2\pi}(1 + \sum_{n=1}^{\infty} 2 \underbrace{\langle v_n^a v_n^b \rangle}_{v_{n\Delta}} \cos(n(\phi_a - \phi_b))), \tag{39}$$

assuming $\psi_a \simeq \psi_b$ in every case.[6] Then, for a single event, a two-particle correlation is obtained as

$$\langle 2 \rangle = v_{n\Delta} = \langle \mathrm{e}^{in(\phi_a - \phi_b)} \rangle = \frac{\sum_{i \neq j}^{M} w_i w_j \mathrm{e}^{in(\phi_i - \phi_j)}}{\sum_{i \neq j}^{M} w_i w_j}, \tag{40}$$

where M is the event multiplicity.

The correlation in Eq. (40) is computed for every event that is to be considered in the analysis. The correlations for the individual events are then averaged. The average for the two-particle correlations is defined as the second order cumulant:

$$c_n\{2\} = \langle \langle 2 \rangle \rangle. \tag{41}$$

Eq. (41) defines the two-particle cumulant for the reference flow, computed from the unidentified background particles. A notation $\{k\}$ is used to indicate a quantity that has been calculated using multi-particle correlations. Here k is the order of the correlation.

As for the event-plane method, a correlation between the particles of interest and the reference is required. The particles satisfying the desired conditions are selected and labeled as POI. The reduced two-particle correlation for a single event is defined as

$$\langle 2' \rangle = \frac{\sum_{i=1}^{m_p} \sum_{j \neq i}^{M} w_j \mathrm{e}^{in(\phi_i - \phi_j)}}{\sum_{i=1}^{m_p} \sum_{j \neq i}^{M} w_j}, \tag{42}$$

[6] There are some fluctuation considerations again, especially when $p_T^a \neq p_T^b$. This is known as the breaking of two-particle factorization, i.e. $V_{n\Delta}(p_T^a, p_T^b) \equiv \langle \mathrm{e}^{in(\phi_a - \phi_b)} \rangle \neq v_n(p_T^a) v_n(p_T^b)$. See [72, 73] for discussion and tests.

where m_p is the number of POI. From this a differential cumulant is obtained as

$$d_n\{2\} = \langle\langle 2' \rangle\rangle, \tag{43}$$

which together with the reference flow cumulant $c_n\{2\}$ gives the final flow coefficient:

$$v_n\{2\} = \frac{d_n\{2\}}{\sqrt{c_n\{2\}}}. \tag{44}$$

Again, if no differential analysis is needed, one has $d_n\{2\} = c_n\{2\}$, and the result may be reduced to $v_n\{2\} = \sqrt{c_n\{2\}}$. Comparing the components in Eq. (44) with the scalar product method Eq. (33) one can see that the methods are essentially equivalent. Only the methods to obtain the coefficients differ. The real advantage of the multi-particle correlations is the inherent mechanism in suppressing the non-flow contributions. The non-flow suppression based on the higher order cumulants will be reviewed next.

Many-Particle Correlations

To suppress the non-flow effects, the scalar product method relied on an η-gap to ensure a proper separation of the subevents. Unlike with the scalar product method, no such gap is applied with the multi-particle correlations. Rather, increasing orders of cumulants reduced by the lower ones [68] is utilized:

$$\begin{aligned} c_n\{2\} &= \langle\langle 2 \rangle\rangle, \\ c_n\{4\} &= \langle\langle 4 \rangle\rangle - 2\langle\langle 2 \rangle\rangle^2, \\ c_n\{6\} &= 1/4(\langle\langle 6 \rangle\rangle - 9\langle\langle 4 \rangle\rangle\langle\langle 2 \rangle\rangle + 12\langle\langle 2 \rangle\rangle^3), \\ &\cdots, \end{aligned} \tag{45}$$

with $v_n\{2\} = \sqrt{c_n\{2\}}$, $v_n\{4\} = \sqrt[4]{-c_n\{4\}}$ and $v_n\{6\} = \sqrt[6]{c_n\{6\}/4}$.

In Eq. (45), each of the orders suppresses the non-flow of the previous one. To see the mechanism behind this, one might write the non-flow explicitly in to the second order cumulant. Redoing the two-particle factorization in Eq. (38) for the second order:

$$\langle \mathrm{e}^{in(\phi_a - \phi_b)} \rangle = \langle \mathrm{e}^{in\phi_a} \rangle \langle \mathrm{e}^{-in\phi_b} \rangle + \delta_2 = v_{n\Delta} + \delta_2, \tag{46}$$

where δ_2 (non-flow) is the correlation term independent of the symmetry plane. The two terms are assumed to be uncorrelated. A second order four-particle factorization can be written as

$$\begin{aligned} \langle \mathrm{e}^{in(\phi_a + \phi_b - \phi_c - \phi_d)} \rangle &= \langle \mathrm{e}^{in\phi_a} \rangle \langle \mathrm{e}^{in\phi_b} \rangle \langle \mathrm{e}^{-in\phi_c} \rangle \langle \mathrm{e}^{-in\phi_d} \rangle \\ &\quad + \langle \mathrm{e}^{in(\phi_a - \phi_c)} \rangle \langle \mathrm{e}^{in(\phi_b - \phi_d)} \rangle \\ &\quad + \langle \mathrm{e}^{in(\phi_a - \phi_d)} \rangle \langle \mathrm{e}^{in(\phi_b - \phi_c)} \rangle + \delta_4 \\ &= v_{n\Delta}^2 + 2(v_{n\Delta} + \delta_2)^2 + \delta_4. \end{aligned} \tag{47}$$

Here angular symmetry between $\phi_a \to \phi_c$ and $\phi_b \to \phi_d$ has been used for combining the factors. Forming the cumulants from equations (46) and (47), and inserting into Eq. (45), one obtains the fourth order cumulant

$$c_n\{4\} = \langle -v_{n\Delta}^2 + \delta_4 \rangle \approx \langle -v_{n\Delta}^2 \rangle \tag{48}$$

where the non-flow of the second order has been suppressed, and the error in the measurements thus reduced.

It is possible to show that the magnitude of the non-flow roughly follows a relation $\delta_{2k} \propto M^{1-2k}$ [68]. For a multiplicity $M = 50 \sim 400$ typical for a heavy-ion collision, the use of a fourth order cumulant as opposed to the second order can significantly reduce the non-flow effects.

Lee-Yang Zeroes

For a reference, a method has been developed to calculate the cumulants to the limit of the infinite order. In the Lee-Yang zeroes method [74, 75], one obtains the reference flow by first computing the generating function

$$G^{\theta}(ir) = \left\langle \prod_{j}^{M} [1 + irw_j \mathrm{e}^{in(\phi_j - \theta)}] \right\rangle \tag{49}$$

for a large number of different real valued $r > 0$ and $0 < \theta < \pi/n$. The flow is given by the estimator

$$v_n\{\infty\} = \frac{1}{N} \sum_{\theta}^{N} \frac{j_{01}}{r_0^{\theta}}, \tag{50}$$

where N is the number of angular samples, j_{01} the first zero of the Bessel function J_0 and r_0^{θ} the first positive minimum of the modulus $|G^{\theta}(ir)|$.

Since only finite order cumulants are used in this analysis, further details will be omitted. For complete details on the method, statistical uncertainty and the extension to differential analysis, see [74, 75].

Explicit methods

A general problem with multi-particle correlations is the required computational effort to calculate the cumulants. Computing a $\{2\}$-correlation from definition (40) is a $\mathcal{O}(\approx n^2)$ operation. For higher orders $\{4\}$, $\{6\}$ etc. the complexity is exponential. Given that the number of events to be analyzed usually varies in the millions, the problem becomes significant. Several ways of approximating Eq. (40) have been introduced over the years [67, 74, 76], all attempting to provide good estimates while minimizing the non-flow and autocorrelations (particles pairing with themselves).

More recently, however, analytical solutions have been presented [77], providing means for fast correlation calculations. The analytical results for higher orders tend to be lengthy, although for two-particle correlations the derivation is compact enough to be shown here. An explicit solution is found by first identifying a relation between the definition Eq. (40) and a Q-vector Eq. (23). By adding the autocorrelation to Eq. (40) one has

$$\sum_{i \neq j}^{M} w_i w_j \langle 2 \rangle + \sum_{k=1}^{M} w_k^2 \underbrace{\mathrm{e}^{in(\phi_k - \phi_k)}}_{=1} = \sum_{i,j=1}^{M} w_i w_j \mathrm{e}^{in(\phi_i - \phi_j)} = |Q_{n,1}|^2, \tag{51}$$

which is solved to get

$$\langle 2 \rangle = \frac{|Q_{n,1}|^2 - \sum_{k=1}^{M} w_k^2}{\sum_{i \neq j}^{M} w_i w_j} = \frac{|Q_{n,1}|^2 - S_{1,2}}{S_{2,1} - S_{1,2}}, \quad S_{b,p} = \left(\sum_{k=1}^{M} w_k^p \right)^b . \tag{52}$$

The cumulant for multiple events is then a weighted average

$$c_n\{2\} = \langle\langle 2 \rangle\rangle = \frac{\sum_{g=1}^{N} \left(\sum_{i \neq j}^{M} w_i w_j \right)_g \langle 2 \rangle_g}{\sum_{g=1}^{N} \left(\sum_{i \neq j}^{M} w_i w_j \right)_g} = \frac{\sum_{g=1}^{N} (|Q_{n,1}|^2 - S_{1,2})_g}{\sum_{g=1}^{N} (S_{2,1} - S_{1,2})_g}, \tag{53}$$

where $g \to N$ loops through the relevant events. The quantity is calculated for the reference particles only, which may also include particles labeled as POI.

The results for the differential cumulants can be derived similarly [77]. For the reduced two-particle correlation

$$\langle 2' \rangle = \frac{p_{n,0} Q_{n,1}^* - s_{1,1}}{m_p S_{1,1} - s_{1,1}}, \quad p_{n,p} = \sum_{k=1}^{m_p} w_k^p \mathrm{e}^{in\phi_k}, \quad s_{b,p} = \left(\sum_{k=1}^{m_q} w_k^p \right)^b . \tag{54}$$

Two additional quantities $p_{n,p}$ and $s_{b,p}$ were defined. Here $p_{n,p}$ is a vector for POI, which may also belong to the reference particles. Only the reference exclusive particles should have a potentially non-unit weight. The scalar quantity $s_{b,p}$ on the other hand is defined for particles strictly *both* POI and reference. The corresponding cumulant is

$$d_n\{2\} = \langle\langle 2' \rangle\rangle = \frac{\sum_{g=1}^{N} \left(\sum_{i=1}^{m_p} \sum_{i \neq j}^{M} w_j \right)_g \langle 2 \rangle_g}{\sum_{g=1}^{N} \left(\sum_{i=1}^{m_p} \sum_{i \neq j}^{M} w_j \right)_g} = \frac{\sum_{g=1}^{N} (p_{n,0} Q_{n,1}^* - s_{1,1})_g}{\sum_{g=1}^{N} (m_p S_{1,1} - s_{1,1})_g}, \tag{55}$$

again where only the relevant events are accounted for. For the final flow coefficient, Eq. (44) is then used.

4 Non-Linear Response

4.1 Response Decomposition

Estimators of Flow

Up to this point the relation between the final state anisotropy and the initial state eccentricities has been described as either linearly (approximate) or non-linearly proportional, without any attempt to explicitly quantify this relation. A general leading-order expansion of a flow observable can be written as a linear combination of n^{th} order harmonic moments, scaled by a set of unknown proportionality constants k_m so that

$$V_n \equiv v_n \mathrm{e}^{in\psi_n} = \sum_{m=0}^{\infty} k_m \varepsilon_n^m \mathrm{e}^{in\Phi_n}, \tag{56}$$

also recalling the participant plane direction Φ_n from section 1.2. However, it has been noted, that such linear combination is in fact not the best representation to describe the relations between initial and final states, particularly concerning the higher harmonic orders [7].

Eq. (56) may act as a starting point for an improved estimate, where in addition to the first order moment an additional (potentially non-linear) term has been introduced [7]:

$$v_n \mathrm{e}^{in\psi_n} = k\varepsilon_n \mathrm{e}^{in\Phi_n} + k'\varepsilon_n' \mathrm{e}^{in\Phi_n'} + \mathcal{E}. \tag{57}$$

Here k and k' are scaling constants, which can be solved for, given the required observables by theoretical simulations. Additionally, $\mathcal{E}$ is a complex error term and $\langle|\mathcal{E}|^2\rangle$ its mean-square, which a good estimator should minimize for the lack of an exact relation. The most suitable estimator for the hydrodynamic response may be chosen from the compatible combinations of low and high order eccentricities in such way that the symmetry properties described in [62] and section 3.1 are preserved. A qualitative analysis of several possible estimators was done in [7].

The results of this analysis are shown in Fig. 10. In the two upper panels for v_2 and v_3, three estimators based on Eq. (57) are presented. The estimators include the basic linear relation $v_n \propto \varepsilon_n$, a relation or two to a projected harmonic $v_n\{\psi_n\} \propto \varepsilon_m\{\Phi_n\}$ of the same direction, and a linear combination of these two. As expected, among the best estimators for the elliptic v_2 and triangular v_3 remain the linear relations to the eccentricity of the same harmonic order:

$$v_2 \mathrm{e}^{in\psi_2} = k\varepsilon_2 \mathrm{e}^{in\Phi_2}, \quad v_3 \mathrm{e}^{in\psi_3} = k\varepsilon_3 \mathrm{e}^{in\Phi_3}. \tag{58}$$

Any other possible alternatives produce no visible improvements. For the higher orders on the other hand, in the two lower panels it is clearly seen that a mere linear relation is insufficient to estimate the resulting flow. The most accurate estimate throughout the whole range of centrality classes is achieved by using a combination of linear and non-linear terms, shown as blue closed circles in Fig. 10. The best estimates for the quadrangular v_4 and pentagonal v_5 (for which the symmetry properties hold) are thus

$$\begin{aligned} v_4 \mathrm{e}^{in\psi_4} &= k\varepsilon_4 \mathrm{e}^{4i\Phi_4} + k'\varepsilon_2^2 \mathrm{e}^{4i\Phi_2}, \\ v_5 \mathrm{e}^{in\psi_5} &= k\varepsilon_5 \mathrm{e}^{5i\Phi_5} + k'\varepsilon_2 \mathrm{e}^{2i\Phi_2} \varepsilon_3 \mathrm{e}^{3i\Phi_3}, \end{aligned} \tag{59}$$

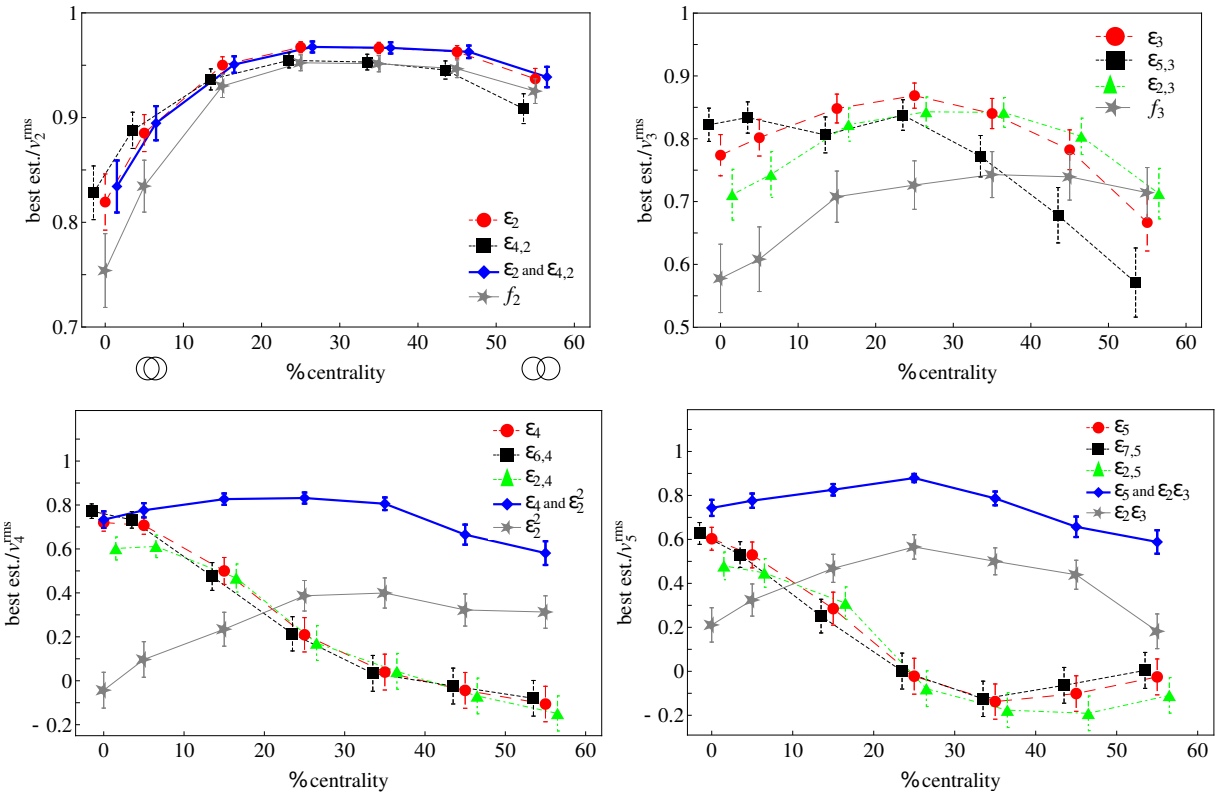

Figure 10: Comparison of various flow estimators for different harmonic orders [7]. A large ratio $k\sqrt{\langle\varepsilon_n^2\rangle/\langle v_n^2\rangle}$ close to unity indicates a low mean-square error, making it a better estimate. The slight drop of v_2 estimation at low centrality classes is due to larger participant area, inducing more fluctuations.

which suggests a low-harmonic ε_n-induced higher order flow. Assuming that a linear relation in Eq. (58) is indeed sufficient for the second and third harmonics, the forms in Eq. (59) are readily presentable as linear and non-linear higher order harmonics decomposed final state flow observables.

Non-Linear Coefficients

Based on the above studies, the hydrodynamic response of higher order eccentricities can be expected to be a superposition of a linear and non-linear contributions. The former is a linear response to the initial eccentricities $v_n \propto \varepsilon_n$, similarly as for the v_2 and v_3. The non-linear contribution on the other hand is supposed to be induced by the lower order harmonics. To formalize this hypothesis, one could write the high harmonics as a sum of two or more terms [12, 78] (by substituting the linear relations into equations in (59) and

their respective higher harmonic counterparts):

$$\begin{aligned}
V_4 &= V_{4L} + \chi_4 V_2^2 \\
V_5 &= V_{5L} + \chi_5 V_2 V_3 \\
V_6 &= V_{6L} + \chi_{62} V_2^3 + \chi_{63} V_3^2 + \chi_{64} V_2 V_{4L} \\
V_7 &= V_{7L} + \chi_7 V_2^2 V_3 + \chi_{74} V_3 V_{4L} + \chi_{75} V_2 V_{5L} \\
V_8 &= V_{8L} + \chi_{82} V_2^4 + \chi_{83} V_2 V_3^2 + \mathcal{E}(V_{4L}, V_{5L}, V_{6L}) \\
&\dots
\end{aligned} \tag{60}$$

Here the χ_n are called the non-linear coefficients, with $\mathcal{E}$ the contribution from higher order linear correlations. For the equations in (60) to be valid, it should hold that the linear part and the non-linearity inducing low harmonic flow are uncorrelated with each other. This correlation is expressed by

$$\frac{\langle V_{4L}(V_2^*)^2\rangle}{\langle V_{4L}\rangle\langle (V_2^*)^2\rangle} \simeq 0, \quad \frac{\langle V_{5L} V_2^* V_3^*\rangle}{\langle V_{5L}\rangle\langle V_2^* V_3^*\rangle} \simeq 0, \quad \cdots \tag{61}$$

where a general test of Pearson correlation $\frac{\langle fg\rangle}{\langle f\rangle\langle g\rangle}$ has been used [79, 84]. Explicitly this can be tested by requiring that

$$\begin{aligned}
\frac{\langle V_4 (V_2^*)^2 v_2^2\rangle}{\langle V_4 (V_2^*)^2\rangle\langle v_2^2\rangle} &= \frac{\langle v_2^6\rangle}{\langle v_2^4\rangle\langle v_2^2\rangle}, \\
\frac{\langle V_5 V_2^* V_3^* v_2^2\rangle}{\langle V_5 V_2^* V_3^*\rangle\langle v_2^2\rangle} &= \frac{\langle v_2^4 v_3^2\rangle}{\langle v_2^2 v_3^2\rangle\langle v_2^2\rangle}.
\end{aligned} \tag{62}$$

Simulation tests of these correlations were done in [79].

The uncorrelation requirements (Eq. (61)) uniquely define the non-linear coefficients. To obtain the coefficients one projects the equations in (60) onto lower harmonics. In this analysis, assuming that the contributions from the higher order linear terms ($V_{4L,5L,\dots}$) are small, only the coefficients for combinations of V_2 and V_3 are considered.

$$\begin{aligned}
\chi_4 &= \frac{\langle V_4 (V_2^*)^2\rangle}{\langle |V_2|^4\rangle} = \frac{v_4\{\Psi_2\}}{\sqrt{\langle v_2^4\rangle}}, & \chi_5 &= \frac{\langle V_5 V_2^* V_3^*\rangle}{\langle |V_2|^2 |V_3^2|\rangle} = \frac{v_5\{\Psi_{23}\}}{\sqrt{\langle v_2^2 v_3^2\rangle}}, \\
\chi_{62} &= \frac{\langle V_6 (V_2^*)^3\rangle}{\langle |V_2|^6\rangle} = \frac{v_6\{\Psi_2\}}{\sqrt{\langle v_2^6\rangle}}, & \chi_7 &= \frac{\langle V_7 (V_2^*)^2 V_3^*\rangle}{\langle |V_2|^4 |V_3^2|\rangle} = \frac{v_7\{\Psi_{23}\}}{\sqrt{\langle v_2^4 v_3^2\rangle}}, \\
\chi_{63} &= \frac{\langle V_6 (V_3^*)^2\rangle}{\langle |V_3|^4\rangle} = \frac{v_6\{\Psi_3\}}{\sqrt{\langle v_3^4\rangle}}, & \chi_{83} &= \frac{\langle V_8 V_2^* (V_3^*)^2\rangle}{\langle |V_2|^2\rangle\langle |V_3|^4\rangle} = \frac{v_8\{\Psi_{23}\}}{\sqrt{\langle v_2^2 v_3^4\rangle}}, \\
\chi_{82} &= \frac{\langle V_8 (V_2^*)^4\rangle}{\langle |V_2|^8\rangle} = \frac{v_8\{\Psi_2\}}{\sqrt{\langle v_2^8\rangle}}, & &\cdots
\end{aligned} \tag{63}$$

Representing the ratio between the non-linear and linear contributions, the coefficients (63) should theoretically be independent of any initial state models and the fluctuations they produce in a given centrality class [12, 14].

4.2 Event-Plane Correlations

Measuring the Mode Coupling

As for the coordinate and momentum space anisotropy magnitudes, a similar relation between their directions is also expected [25]. For low harmonic orders, notably when $v_n \propto \varepsilon_n$, their respective symmetry planes ψ_n and participant planes Φ_n are found to be aligned. However, for higher orders $n > 3$ and sufficiently large eccentricities, the relation is violated. A measurement of correlations between the event planes can provide insight on how the higher order directions may depend on those of the lower ones.

Having measured the flow with respect to other directions, the following correlations also provide means to measure the relation between event plane directions and their fluctuations. In order to measure these correlations, a Pearson correlation is calculated, i.e. a ratio between the respective flow coefficients:

$$\begin{aligned}
\rho_4 &= \frac{\mathrm{Re}\langle V_4 (V_2^*)^2 \rangle}{\sqrt{\langle |V_4|^2 \rangle \langle |V_2|^4 \rangle}} = \frac{v_4\{\psi_2\}}{v_4\{\psi_4\}}, \quad \rho_5 = \frac{\mathrm{Re}\langle V_5 V_2^* V_3^* \rangle}{\sqrt{\langle |V_2|^2 |V_3|^2 \rangle \langle |V_5|^2 \rangle}} = \frac{v_5\{\psi_{23}\}}{v_5\{\psi_5\}}, \\
\rho_{62} &= \frac{\mathrm{Re}\langle V_6 (V_2^*)^3 \rangle}{\sqrt{\langle |V_6|^2 \rangle \langle |V_2|^6 \rangle}} = \frac{v_6\{\psi_2\}}{v_6\{\psi_6\}}, \quad \rho_7 = \frac{\mathrm{Re}\langle V_7 (V_2^*)^2 V_3^* \rangle}{\sqrt{\langle |V_2|^4 |V_3|^2 \rangle \langle |V_7|^2 \rangle}} = \frac{v_7\{\psi_{23}\}}{v_7\{\psi_7\}}, \\
\rho_{63} &= \frac{\mathrm{Re}\langle V_6 (V_3^*)^2 \rangle}{\sqrt{\langle |V_6|^2 \rangle \langle |V_3|^4 \rangle}} = \frac{v_6\{\psi_3\}}{v_6\{\psi_6\}}.
\end{aligned} \tag{64}$$

Generally, a value close to unity indicates a strong correlation, whereas a zero value indicates the opposite. Despite the name "event-plane correlation", it is worth noting that the quantities are in fact correlations between different flow magnitudes, only with respect to directions of lower harmonic event-planes. The maximum v_n can be found in the direction of its own event plane, which implies that $v_n\{\psi_n\} \geq v_n\{\psi_m\}$ always when $n \neq m$. Generally, following the inequalities, ρ_n is always below unity, and for uncorrelated quantities the correlation will be zero.

There have been previous event plane measurements [33, 34]. Measurement of these quantities was also done in this analysis, but not as the focus of this thesis. Results for the event plane correlations will be provided in appendix A.1.

5 Measurements

5.1 Experimental Setup

Data Analysis

This analysis uses the experimental data recorded by ALICE in Pb–Pb collisions at the center-of-mass energy $\sqrt{s_{\mathrm{NN}}} = 2.76\,\mathrm{TeV}$ during the 2010 heavy-ion run at the LHC. Detailed description of the ALICE detector can be found in [80–82]. See Table 2 for a summary of default track selection and cut settings. Event triggering was done using the V0 scintillator counters, the V0-A and V0-C arrays [80, 83]. A combination of Inner Tracking System (ITS) [80] and Time Projection Chamber (TPC) [80] was used for the track and primary vertex reconstruction. A distance less than 10 cm was required between the primary vertex and nominal interaction point (Z-vertex cut of $\pm 10\,\mathrm{cm}$). Pile-up events resulting from the detector dead time were rejected. For the centrality determination, information from the V0 arrays was used. More details on centrality determination will be given in the next section.

Only charged particles are used for the results. In order to avoid large contributions from secondary vertices, the tracks reconstructed were required to have a distance of closest approach to the primary vertex of less than 3.2 cm and 2.4 cm in the longitudinal (z) and transverse directions, respectively. For each track at least 70 TPC space points were required. A pseudorapidity gap $|\Delta\eta| \geq 0.8$ was applied between the correlated particles (scalar product subevents), suppressing the non-flow effects. In practical terms, only tracks within the subset region $\eta \in \pm[0.4, 0.8]$ were accepted. Furthermore, the track selection was limited to transverse momentum range $0.2 < p_T < 5.0\,\mathrm{Gev/c}$.

For the hydrodynamic comparisons, calculations from `VISH2+1` [84] and `IP-Glasma+MUSIC+UrQMD` [85] featuring varying initial geometry models are used. Hydrodynamic calculations are presented whenever available. The AMPT data was taken from the ALICE simulation production. In each configuration, the AMPT uses the same global parameters $\alpha_s = 0.33$ and a partonic cross section of 1.5 mb. For the Lund string fragmentation, the respective parameters were $\alpha_s = 0.5$ and $b = 0.9\,\mathrm{GeV}^{-2}$.

Centrality Determination

The centrality determination is based on the observed event multiplicity. Because the actual details depend on the general experiment, a short introduction to centrality determination in the ALICE experiment [21] will be given here.

Table 2: Event selection

	Data
Z-vertex cut	$-10\,\mathrm{cm} < Z_{\mathrm{vtx}} < 10\,\mathrm{cm}$
Track selection bit	TPC only
Subset region (η)	$-0.8 \sim -0.4$ and $0.4 \sim 0.8$
Particle selection	All charged
p_T-cut	$0.2 < p_T < 5.0\,\mathrm{GeV}/c$

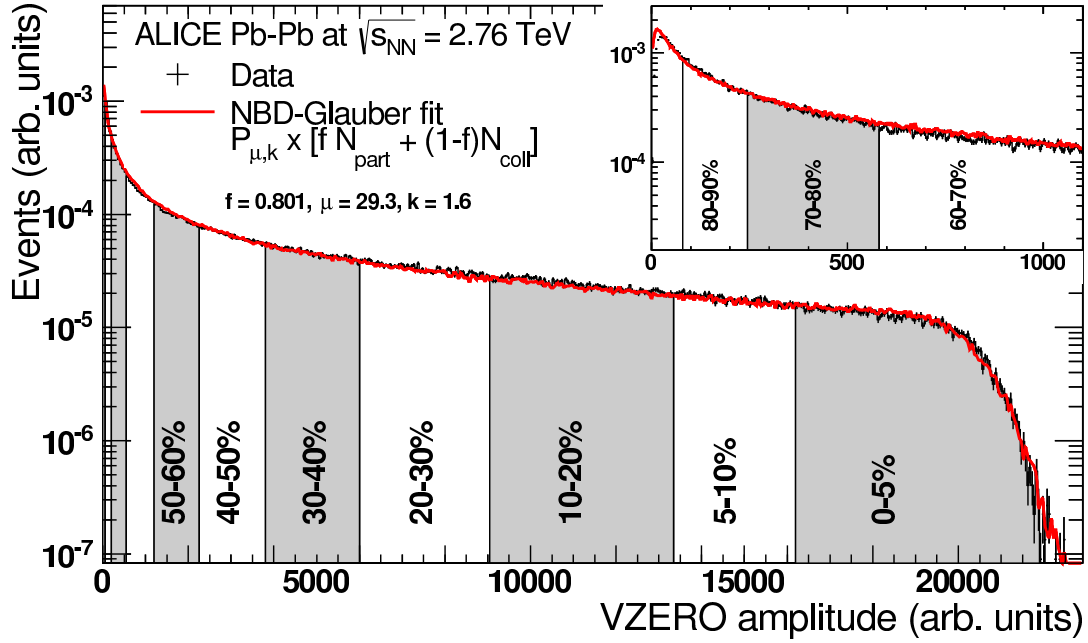

Figure 11: The multiplicity distribution as a sum of V0 amplitudes [21], proportional to the event multiplicity. Centrality classes are given by the participant count from the Glauber model, after fitting the model calculations to the measured data. Some details of the procedure are given in the text.

Experimentally the collisions are grouped into centrality bins, arranged by the amount of overlap in the collision geometry. A high multiplicity in a collision event implies a larger participant count, further translating into a large geometric overlap. In addition to participant counts, the centrality is also expressed with a centrality percentile, with low numbers indicating a high centrality.

The number of participants in a collision event can be estimated by fitting results from Glauber model simulations to the real world measurements [21]. For each event, the Glauber model gives the number of participants N_{p} and binary collisions N_{c}. Together these are parameterized to give a number of independently emitting particle sources, the so called "ancestors":

$$N_{\mathrm{a}} = fN_{\mathrm{p}} + (1-f)N_{\mathrm{c}}, \tag{65}$$

where f is a parameter obtained by fitting to experimental data. For each ancestor, the contribution as a number of hits in the detector is estimated. The probability to count n hits is given by the negative binomial distribution

$$P_{\mu,k}(n) = \frac{\Gamma(n+k)}{\Gamma(n+1)\Gamma(k)} \cdot \frac{(\mu/k)^n}{(\mu/k+1)^{n+k}}, \tag{66}$$

where μ and k are parameters to control the mean multiplicity per ancestor and the width of the distribution, respectively. To get the total multiplicity of the collision event, the distribution in Eq. (66) is sampled N_{a} times.

A Glauber model fit to the data is presented in Fig. 11. The V0 amplitude, proportional to the event multiplicity, defines the horizontal axis. By varying the parameters

Table 3: Centrality classes for the impact parameter.

Centrality(%)	b(fm)
0-5	0.00-3.50
5-10	3.50-4.94
10-20	4.94-6.98
20-30	6.98-8.55
30-40	8.55-9.81
40-50	9.81-11.04
50-60	11.04-12.09
60-70	12.09-

of the distribution, one may match the Glauber data to the measurements, giving the number of participant nuclei. From the number of participants one may then get the impact parameter b to be used in defining the centrality classes, also seen in Table 3.

5.2 Systematics

Non-Linear Coefficients

Several different analysis configurations were used to evaluate the systematics. For each configuration, the default reference setup was modified to give an alternative set of results, one set for each modification. The alternative results were then compared to the results given by the default setup, yielding a table of relative errors. For the total systematic error, the errors from the individual checks were quadratically summed. The systematic checks for the non-linear coefficients are summarized in table 4.

In table 4, the systematic checks have been categorized to four different groups. Tracking related errors have been identified by comparing the selection of events from the two magnetic field polarities. With both of the polarities, the number of events reconstructed were nearly identical. Other checks include the efficiency correction for detector limitations, and the track filtering in an attempt to reduce the unwanted background. In the final analysis, only charged particles contribute to the results. To see how the correlation of charge combinations induces non-flow contributions, another check was established. Compared to the default setup where both negative and positive charges are considered, individual combinations of the same charge signs were also analyzed.

The rest of the checks cover the event-related uncertainties. This includes the alteration of the primary vertex reconstruction range (z-vertex cut) to ± 8 cm and the centrality determination using either SPD or TRK reconstruction (silicon pixel detector and TPC tracking, respectively). The Z-vertex check was used to test the longitudinal detector efficiency. To observe the effect of the beam related background, another set was measured with the high multiplicity outliers removed.

For the fourth harmonic coefficient χ_4 the systematic uncertainties are generally small. The most notable error here comes from the individual sets of events from magnetic field polarities and charged particle sign restrictions. For the event-related uncertainties, comparison between the different systematic configurations show practically no difference. For the higher orders the pattern of uncertainties is roughly same, even if the error gets

Table 4: Overall χ_n systematics. The overall total is a quadratic sum of all the individual checks.

Type [%]	χ_4	χ_5	χ_{62}	χ_{63}
Tracking				
Track filter bit selection	< 1	< 1	6.2	9.3
Efficiency correction	< 1	< 1	< 1	3.6
Magnetic field polarization (+)	1.2	1.8	12.5	3.8
Magnetic field polarization (−)	1.5	1.7	4.5	4.1
Event Selection				
Z-vertex cut	< 1	< 1	3.4	3.2
High multiplicity outliers	< 1	< 1	2.1	2.7
Correlations				
Charge combination (− −)	2.5	9.9	7.7	11.9
Charge combination (+ +)	2.5	4.9	8.8	5.7
Centrality Determination				
Centrality determination (SPD)	< 1	< 1	2.2	6.0
Centrality determination (TRK)	< 1	< 1	3.5	4.1
Overall $(\sum_i \delta_i^2)^{\frac{1}{2}}$	4.2	11.3	19.6	19.4

slightly larger. The larger error is a result of a smaller v_n, for which the results become more sensitive to azimuthal modulation due to detector imperfections.

5.3 Results

Non-Linear Coefficients

The non-linear response coefficients χ_n are shown in Fig. 12. Looking at the data, one may first note the centrality dependence of the coefficients. The centrality dependence is especially evident for χ_4 and χ_{62}. For χ_4, the non-linear contribution slightly peaks for the lowest centrality class, proceeding to steadily decrease towards the higher centralities. In the limits of the statistical error, the decrement of χ_{62} seems to be slightly stronger. The centrality dependence does seem to hold also for χ_5, although clearly only for the mid-centrality classes.

Generally, all of the coefficients are observed to be decreasing for more peripheral collisions. An exception to this is χ_{63}, where the placement of the data points suggest little to no variation over the centrality classes. However, the statistical fluctuations prevent any definite conclusions. For each of the coefficients, the data points are above one, indicating the non-linear response to be the dominant component. Furthermore, the non-linear contribution is considerably higher for χ_5 than the rest of the coefficients.

The data is then compared to viscous hydrodynamical calculations. Calculations from two separate models are presented, with total of three different initial condition models. In Fig. 13, the red and blue bands represent the `VISH2+1` [84] calculations with MC-Glauber and MC-KLN initial conditions, and with $\eta/s = 0.08$ and 0.20. `IP-Glasma+MUSIC+UrQMD`

[85] with $\eta/s = 0.095$ is shown in yellow.

The data for χ_4 in the first panel of Fig. 13 is clearly the best described by the calculations using VISH2+1 MC-KLN and IP-Glasma+MUSIC+UrQMD. The calculations using VISH2+1 MC-Glauber seem to overestimate the non-linear contribution. They also fail to reproduce the centrality dependence in more central collisions. For χ_5, in every model the agreement with the data is slightly worse compared to χ_4, although the centrality dependence seems to be well captured with every calculation. In every case, the calculations have resulted in an overestimation in almost every centrality class. Only VISH2+1 calculations with $\eta/s = 0.20$ are still mostly within the systematic error limits.

Moving up to higher orders, the difference between the calculations for χ_{62} is larger. On average, between all the centrality classes the calculations from VISH2+1 MC-KLN show the best agreement. Meanwhile, calculations from the same model with MC-Glauber completely fail to reproduce the data. In low centrality classes, IP-Glasma+MUSIC+UrQMD overestimates the non-linear contribution. The agreement between the different models becomes better for χ_{63}. For χ_{63}, higher viscosity seems to be preferred from the data viewpoint. All of the calculations show a clear centrality dependence, with calculations with lower viscosity yielding a larger non-linearity. In the data this centrality dependence was not observed, although the large statistical error prevented any definite conclusions.

From the upper panels of Fig. 13, specifically the results from VISH2+1, one may also observe the sensitivity of the coefficients to the initial conditions. Especially χ_5 and χ_{63} seem to be independent of the initial conditions. While χ_4 does not clearly show this behaviour, it seems to be insensitive to viscous effects, making it in turn possibly useful for constraining initial state related properties. On the third panel, one also observes that χ_{62} is sensitive to both the initial conditions and shear viscosity. In every case whenever there is a sensitivity to viscosity, more viscous calculations seem to reduce the non-linear

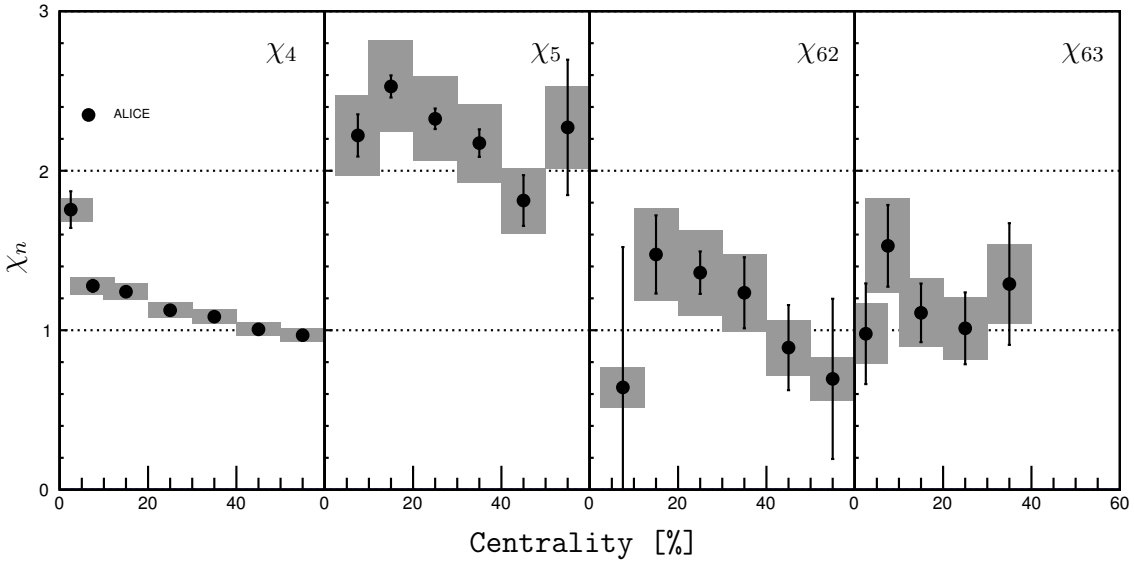

Figure 12: Non-linear response coefficients, as a function of collision centrality. The systematic errors are visualized as gray boxes, while the error bars represent the statistical uncertainty.

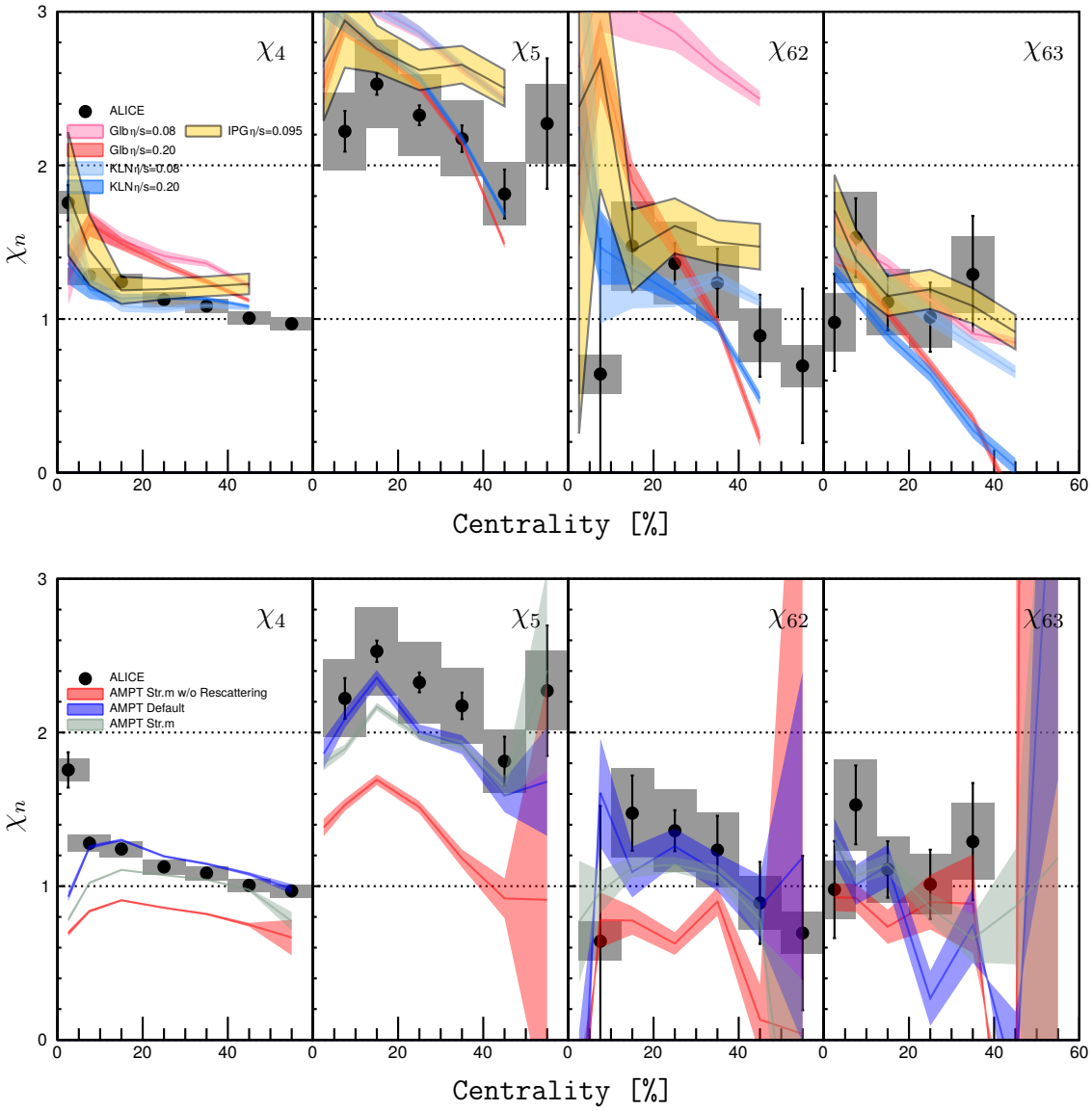

Figure 13: Data comparison to hydrodynamics and AMPT calculations. For the hydrodynamic comparisons two sources were used: `VISH2+1` MC-Glauber and MC-KLN [84] as the red and blue colored bands, respectively, and [85] for `IP-Glasma+MUSIC+UrQMD` in yellow.

contribution.

As for the results obtained with AMPT, presented in the lower panel of Fig. 13, the default and the string melting configurations with rescattering are generally seen to reproduce the data best. For χ_4, the agreement is very good, except for the lowest centrality class where the data is significantly underestimated. Looking at χ_5, the magnitude of non-linear contribution and centrality dependence are both well reproduced within the error limits. Similar observations can be made for the χ_{62}. Only for χ_{63} the calculations remain unclear in mutual agreement. In every case it can be concluded that the hadronic interactions are non-negligible as leaving out the rescattering phase seems to result in

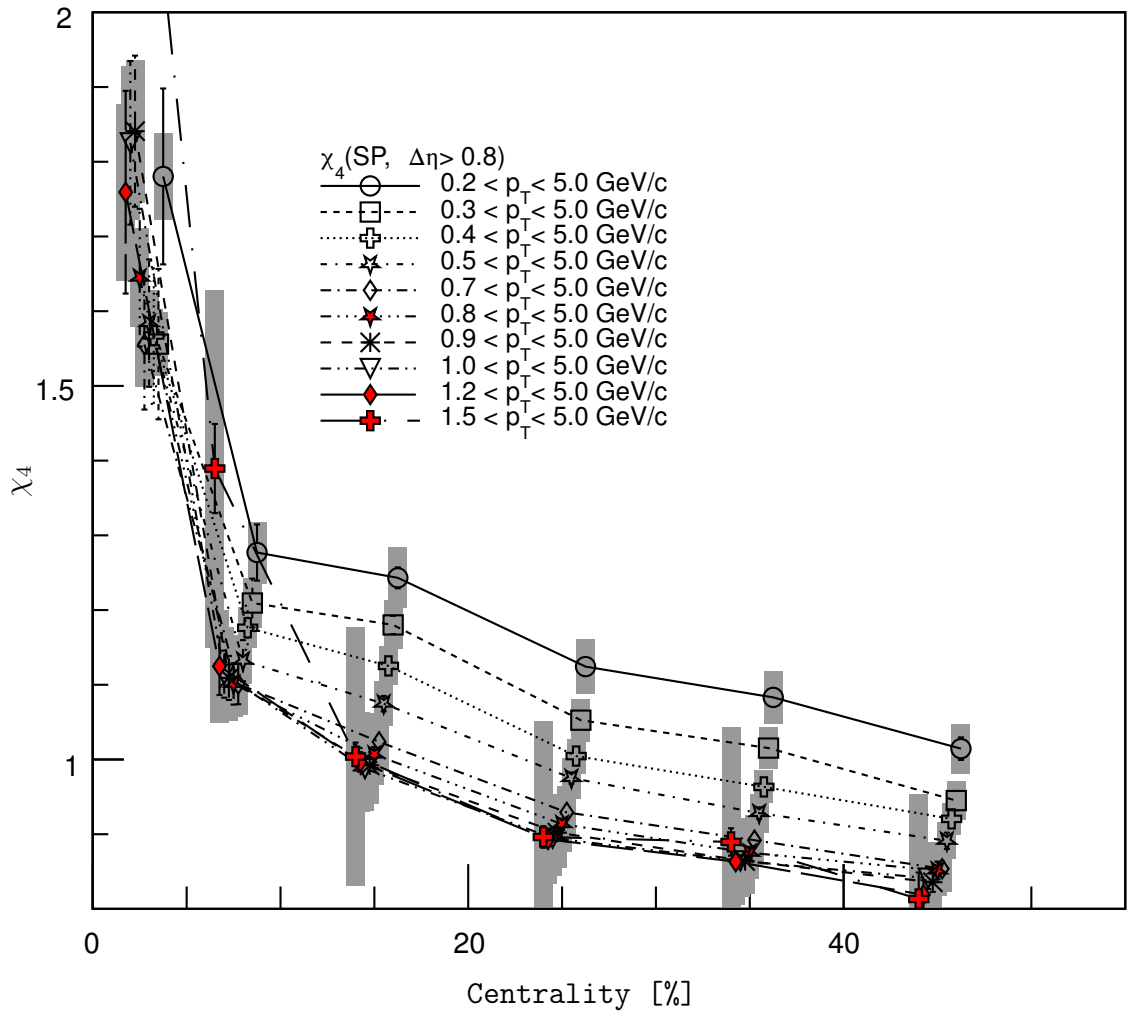

Figure 14: The p_T dependence of χ_4. For statistical reasons the upper bound for the p_T-cuts are kept constant over the bins, while gradually increasing the minimum bound.

a large underestimation. However, rescattering does not seem to affect the centrality dependence of the results.

Transverse Momentum Dependence

The transverse momentum dependence of χ_4 has also been studied. No differential analysis was performed, but rather restricting the particle selection by rejecting low-p_T particles from a gradually narrowed momentum subset region. By examining Fig. 14, it is clear that the non-linear response is p_T-dependent, at least for the lower p_T-cuts. For higher cuts the dependency is much less evident. Studying the p_T-dependence of the observables can help understand the viscous correction to the momentum distribution at the hadronic freeze-out, which is among the least understood parts of the hydrodynamic calculations [12, 19].

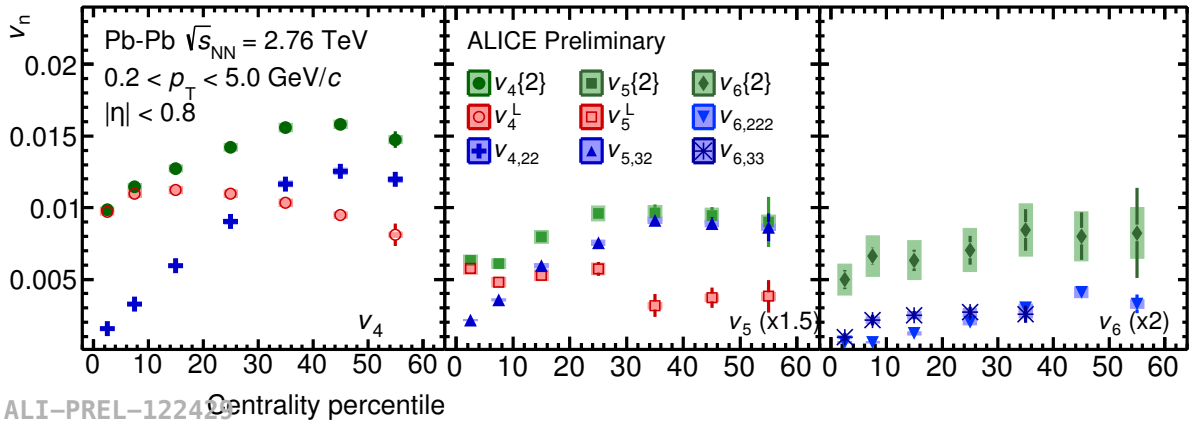

Figure 15: Magnitudes of the linear and non-linear contributions (ALICE preliminary).

Flow Contributions

Finally, Fig. 15 shows the contributions of linear and non-linear response separately for v_4, v_5 and v_6. The non-linear contribution is low for the central collisions, especially in case of v_4, where the linear part makes up for most of the contribution. As the centrality increases, the contribution of the non-linear response also increases significantly. It is also worth noting that as is the case for odd harmonics, the non-linear part clearly dominates in v_5 for the majority of centrality classes, implying that this is mostly induced by the low-order harmonics.

6 Summary

The final state flow of the higher harmonics can be decomposed into linear and non-linear contributions, with respect to the initial state eccentricities. The linear part is expected to be directly proportional to the eccentricities of the same harmonic, while the non-linear part emerges as a contribution induced by the lower harmonic flows. The resulting decomposition could then be expressed with a set of non-linear coefficients, χ_n. One of the major implications of this decomposition is that the resulting coefficients should be less sensitive to the initial conditions.

A brief introduction was given to some of the relevant topics in the field of heavy-ion physics. Among these topics two major theoretical models, AMPT and the hydrodynamical model, were briefly reviewed. The experimental flow analysis and the details of the non-linear decomposition were also discussed. However, the primary purpose of this thesis was to present the first real measurements of these coefficients. The measurements were carried out for several new observables with a wide range of systematic checks.

The non-linear coefficients were measured from ALICE lead-lead collisions at $\sqrt{s_{NN}} = 2.76\,\text{TeV}$. All of the results were obtained using the generalized scalar product method. Comparisons to AMPT and hydrodynamical model calculations are provided. No perfect agreement in the comparisons is observed, although some of the theoretical calculations reproduce to the measurements quite well.

The non-linear coefficients are noted to be centrality dependent. Of these coefficients χ_4 and χ_{62} are shown to feature the largest dependence, while for the χ_5 and χ_{62} centrality dependence is less evident. The centrality dependence and the magnitude of these two vary a lot depending on the chosen initial conditions and η/s. A clear transverse momentum dependence is also observed for χ_4. At low p_T the dependence is more prominent, while for the higher cuts this dependency vanishes. Transverse momentum studies might further advance the understanding of viscous corrections to the hadronic freeze-out. Further studies may also consider the other coefficients when measuring the relations to the transverse momentum.

A comparison between various theoretical models, especially when considering their initial states, has provided insight about different sensitivity of these coefficients to both the initial conditions and/or η/s. For example, it was clearly observed that the χ_5 and χ_{63} are indeed independent of the initial conditions. Given that the initial state uncertainty can be removed, using the experimental data it is now possible to better constrain the parameters relating to the QGP interaction strength and patterns.

A Appendix

A.1 Additional Measurements

Event Plane Correlations

The correlation between event planes is measured with a Pearson ratio $v_n\{\psi_m\}/v_n\{\psi_n\}$. Results of such a measurement is presented in Fig. 16. In all cases the ratio is below unity, as expected. Generally, the closer to the peripheral region, the more the event planes are correlated. In a peripheral collisions, the data for ρ_4 (notated as ρ_{422} in the ALICE preliminary results) suggests a high correlation between the directions ψ_2 and ψ_4. This behaviour is also observed for ρ_{523} (ρ_{532}) and ρ_{62} (ρ_{6222}), even if the ψ_{62} correlation isn't as strong. As for the ρ_{63} (ρ_{633}), there is no clear centrality dependence. The pattern of uncertainties for the event plane correlations (results in the appendix) roughly follows those of the non-linear coefficients. The measurements are seen to be compatible with the previous event plane measurements [33].

Flow Coefficients

We test the correctness of our basic analysis by plotting and comparing our new flow measurements. In Fig. 17, plots of individual flow coefficients are shown. These coefficients have been compared to previous ALICE measurements from [86] where the experimental setup is mostly identical. Two different methods were used to compute the coefficients, the scalar product method (SP) and the multi-particle correlations (more specifically Q-cumulants or QC). For all harmonics, we have calculated the ratio between the QC and SP results. As expected from the equivalence of the two methods, no significant differences are seen, apart from the statistical variations from correlations between likely different particles. In our analysis, we mainly utilize the scalar product method, as explained in previous sections.

The measured SP v_n also presented in Fig. 18. Four different coefficients from v_2 to v_5 are shown. On the left panel (A)–(C), the centrality dependence is shown (as in Fig. 17, excluding the fifth order harmonic). On the right side (a)–(c), the coefficients are presented as a function of $p_{T,\mathrm{min}}$ where for each successive bin the p_T-cut has been narrowed by some margin (similar to Fig. 14 in section 5.3).

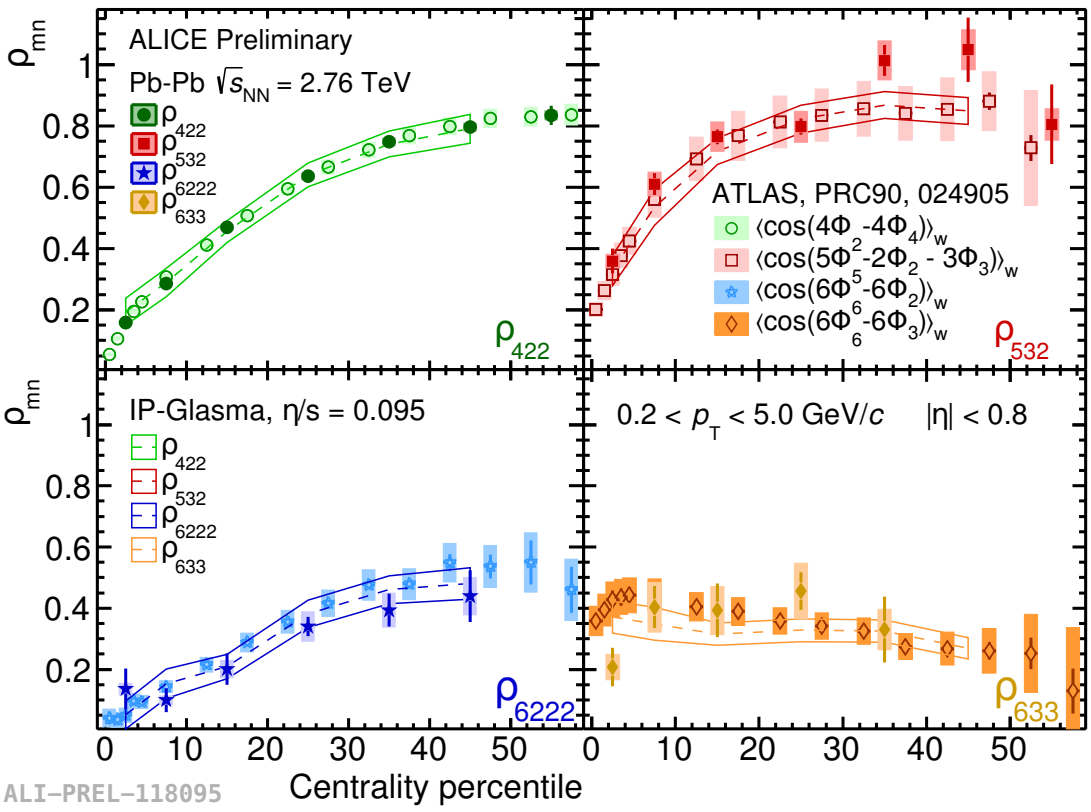

Figure 16: Event plane correlations, as a function of collision centrality (ALICE preliminary). Comparison to ATLAS data points is provided [33].

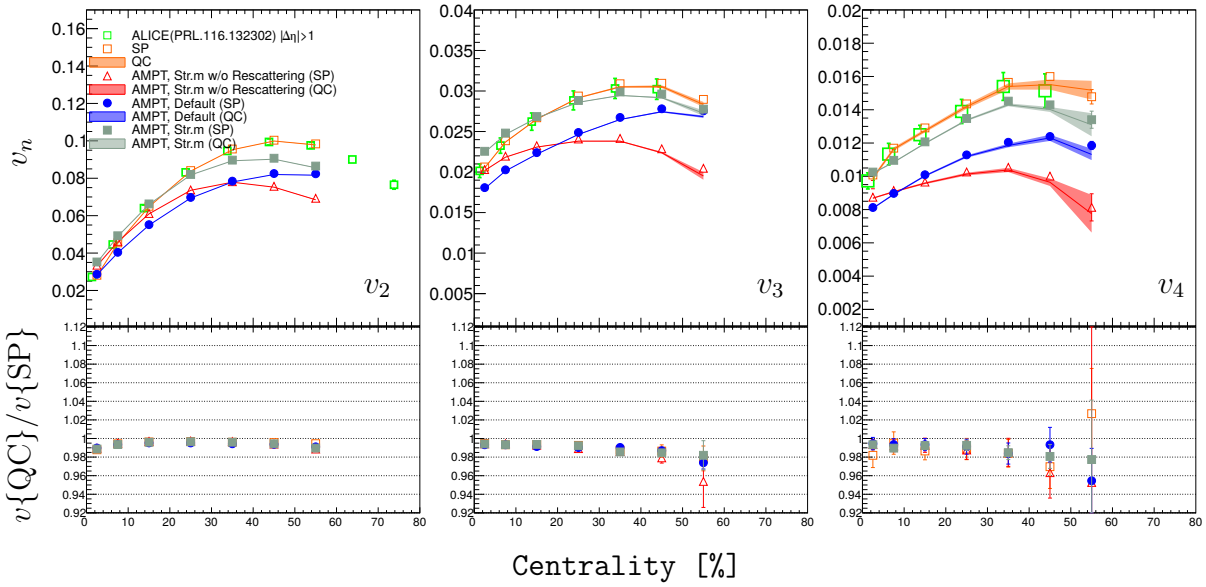

Figure 17: Flow coefficients as a function of centrality. Previously published ALICE measurements are used as a reference [86]. The ratio compares the potential differences between the coefficients calculated with either the SP or QC method. In the figure, SP results are displayed with data points while the QC is shown as bands.

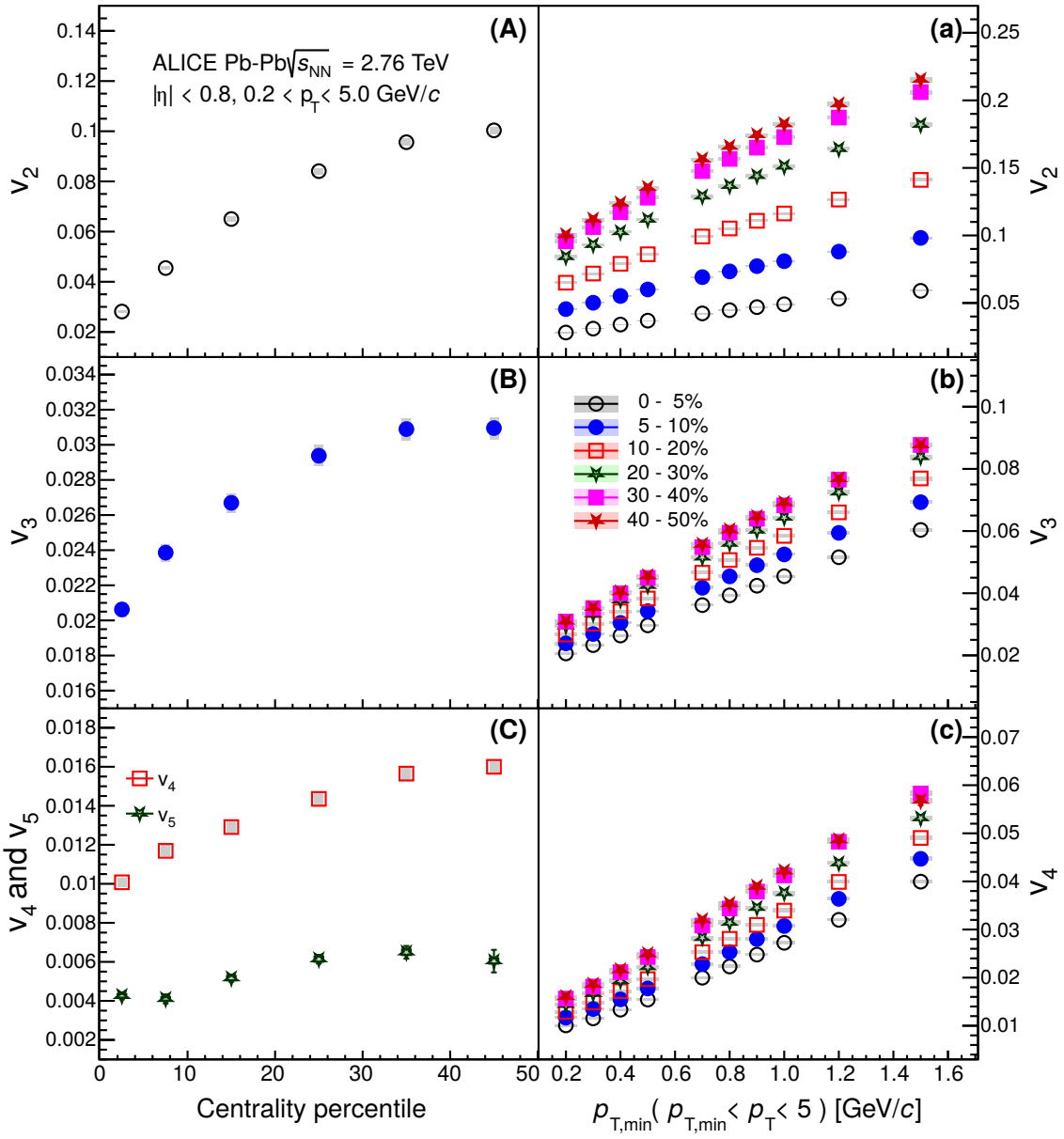

Figure 18: Flow coefficients as a function of centrality and $p_{T,\mathrm{min}}$. The results are for the measured SP only.

References

[1] E.J. Lofgren, ACCELERATOR DIVISION ANNUAL REPORTS, 1 JULY 1972 12/31/1974. - Report Number: LBL-3835 (1975) `https://publications.lbl.gov/islandora/object/ir%3A102869` (cited 1.1.2017)

[2] A.D. Kovalenko, Status of the Nuclotron, EPAC'94, London, June 1994. Proceedings, v.1, p.p. 161-164, (1995)

[3] G. Martinez, Advances in Quark Gluon Plasma (2013) arXiv:1304.1452v1 [nucl-ex]

[4] U. Heinz, M. Jacob, preprint (2000) arXiv:nucl-th/0002042

[5] [PHENIX collaboration], *Nucl.Phys.* **A757** 184-283 (2005) arXiv:nucl-ex/0410003

[6] [STAR collaboration], *Nucl.Phys.* **A757** 102-183 (2005) arXiv:nucl-ex/0501009v3

[7] F.G. Gardim *et al.*, *Phys.Rev.* **C85** 024908 (2012) arXiv:1111.6538 [nucl-th]

[8] B.H. Alver *et al.*, *Phys.Rev.* **C82** 034913 (2010) arXiv:1007.5469v2

[9] C. Gale *et al.*, *Int.J.Mod.Phys.* **A28** 1340011 (2013) DOI:10.1142/S0217751X13400113

[10] H. Song *et al.*, *Phys.Rev.Lett.* **106** 192301 (2011) arXiv:1011.2783v2

[11] H. Song *et al.*, *Phys.Rev.* **C83** 054910 (2011) arXiv:1101.4638v2

[12] D. Teaney, Li Yan, *Phys.Rev.* **C86** 044908 (2012) arXiv:1206.1905 [nucl-th]

[13] D. Teaney, Li Yan, *Phys.Rev.* **C90** 024902 (2014) DOI:10.1103/PhysRevC.90.024902

[14] Li Yan, J.-Y. Ollitrault, *Phys.Lett.B* **744** 82-87 (2015) arXiv:1502.025021v1 [nucl-th]

[15] R.A. Lacey *et al.*, *Phys.Rev.Lett.* **98** 092301 (2007) arXiv:nucl-ex/0609025

[16] R. Gupta, Introduction to Lattice QCD - Report Number: LAUR-98-3174 (1997) arXiv:hep-lat/9807028

[17] P. Romatschke, *Int.J.Mod.Phys.* **E19** 1-53 (2010) arXiv:0902.3663v3

[18] U.W. Heinz, J. Liu, *Nucl.Phys.A* **956** 549 (2016) arXiv:1512.08276v2

[19] H. Niemi, K. J. Eskola, R. Paatelainen, *Phys.Rev.* **C93** 024907 (2016) arXiv:1505.02677 [hep-ph]

[20] M.L. Miller *et al.*, *Ann.Rev.Nucl.Part.Sci.* **57** 205-243 (2007) arXiv:nucl-ex/0701025

[21] [ALICE collaboration], *Phys.Rev.* **C88** 044909 (2013) arXiv:1301.4361v3 [nucl-ex]

[22] D. Teaney, Li Yan, *Phys.Rev.* **C83** 064904 (2011) DOI

[23] M. Miller, R. Snellings, Eccentricity fluctuations and its possible effect on elliptic flow measurements (2003) arXiv:nucl-ex/0312008v2

[24] [PHOBOS collaboration] *Phys.Rev.Lett.* **98** 242302 (2007) arXiv:nucl-ex/0610037

[25] Z. Qiu, U.W. Heinz, *Phys.Rev.* **C84** 024911 (2011) arXiv:1104.0650v3 [nucl-th]

[26] T. Hirano *et al.*, *Phys.Lett.B636* **299** (2006), arXiv:nuclth/0511046 [nucl-th]

[27] B. Schenke, P. Tribedy and R. Venugopalan, *Phys.Rev.Lett.* **108** 252301 (2012), arXiv:1202.6646 [nuclth]

[28] B. Schenke, P. Tribedy and R. Venugopalan, *Phys.Rev.* **C86** 034908 (2012), arXiv:1206.6805 [hep-ph]

[29] S.A. Voloshin *et al.* (2008) arXiv:0809.2949v2

[30] B.H. Alver, G. Roland, *Phys.Rev.* **C81** 054905 (2010) arXiv:1003.0194v3

[31] H. Niemi *et al.*, *Phys.Rev.* **C87** 054901 (2013) arXiv:1212.1008v1

[32] J. Fu, *Phys.Rev.* **C92** 024904 (2015) DOI:10.1103/PhysRevC.92.024904

[33] [ATLAS collaboration], *Phys.Rev.* **C90** 024905 (2014) arXiv:1403.0489

[34] [CMS collaboration], *Phys.Rev.*, **C89** 044906 (2014) arXiv:1310.8651

[35] E. Fermi, *Prog.Theor.Phys* **5** 570 (1950) DOI:10.1143/ptp/5.4.570

[36] L. Landau, *Izv.Akad.Nauk Ser.Fiz* **17** 51 (1953)

[37] I. Khalatnikov, *Zh.Eksp.Teor.Fiz* **27** (1954)

[38] M.H. Thoma, M. Gyulassy, *Nucl.Phys.B* **351** 491 (1991)

[39] P. Danielewicz, M. Gyulassy, *Phys.Rev.* **D31** 53 (1985) DOI:10.1103/PhysRevD.31.53

[40] P. Kovtun *et al.*, *Phys.Rev.Lett.* **94** 111601 (2005) arXiv:hep-th/0405231v2

[41] J.A. Font *et al.*, *Phys.Rev.* **D61** 044011 (2000) arXiv:gr-qc/9811015

[42] H.-J. Drescher *et al.*, *Phys.Rev.* **C74** 044905 (2006) arXiv:nuclth/0605012 [nucl-th]

[43] C. Shen *et al.*, *J.Phys.* **G38** 124045 (2011), arXiv:1106.6350 [nucl-th]

[44] [STAR collaboration], *Phys.Rev.* **C79** 034909 (2009), arXiv:0808.2041v2

[45] C. Gale *et al.*, *Phys.Rev.Lett.* **110** 012302 (2013), arXiv:1209.6330 [nucl-th]

[46] F. Cooper, G. Frye, *Phys. Rev.* **D10** 186 (1974)

[47] C. Hung, E.V. Shuryak, *Phys.Rev.* **C57** 1891 (1998) arXiv:hep-ph/9709264

[48] H. Holopainen, P. Huovinen, *J.Phys.Conf.Ser.* **389** 012018 (2012) arXiv:1207.7331 [hep-ph]

[49] Z.-W. Lin *et al.*, *Phys.Rev.* **C72** 064901 (2005) arXiv:nucl-th/0411110

[50] J. Xu, C.M. Ko, *Phys.Rev.* **C83** 034904 (2011) arXiv:1101.2231 [nucl-th]

[51] B. Zhang, *Comput.Phys.Commun.* **109** 193 (1998)

[52] X.-N. Wang, *Phys.Rev.* **D43** 104 (1991)

[53] X.-N. Wang, M. Gyulassy, *Phys.Rev.* **D44** 3501 (1991)

[54] J.D. Bjorken, *Phys.Rev.* **D27** 140 (1983) DOI:10.1103/PhysRevD.27.140

[55] T. Sjostrand, *Comput.Phys.Commun.* **82** 74 (1994)

[56] B.-A. Li, C.M. Ko, *Phys.Rev.* **C52** 2037 (1995) DOI:10.1103/PhysRevC.52.2037

[57] B. Li, *et al.*, *Int.J.Mod.Phys.* **E10** 267 (2001)

[58] S. Voloshin, Y. Zhang, *Z.Phys.* **C70** 665-672 (1996)

[59] J.-Y. Ollitrault, *et al.*, *Phys.Rev.* **C80** 014904 (2009) arXiv:0904.2315v3

[60] A.M. Poskanzer, S.A. Voloshin, *Phys.Rev.* **C58** 1671-1678 (1998) arXiv:nucl-ex/9805001v2

[61] J. Jia, S. Mohapatra, *Eur.Phys.J.* **C73** 2510 (2013) arXiv:1203.5095v3

[62] M. Luzum, *J.Phys.G* **38**, 124026 (2011) arXiv:1107.0592 [nucl-th]

[63] C. Adler *et al.*, *Phys.Rev.* **C66** 034904 (2002) 10.1103/PhysRevC.66.034904

[64] [PHENIX collobration] *Phys.Rev.Lett.* **91** 182301 (2003) arXiv:nucl-ex/0305013v2

[65] [PHOBOS Collaboration] *Phys.Rev.* **C81** 034915 (2010) arXiv:1002.0534v3

[66] M. Luzum, J.-Y. Ollitrault, *Phys.Rev.* **C87** 044907 (2013) arXiv:1209.2323v3

[67] N. Borghini *et al.*, *Phys.Rev.* **C63** 054906 (2001) arXiv:nucl-th/0007063v3

[68] N. Borghini *et al.*, *Phys.Rev.* **C64** 054901 (2001) arXiv:nucl-th/0105040v2

[69] P. Danielewicz, G. Odyniec, *Phys.Lett.B* **157** 146 (1985)

[70] [STAR collaboration], *Phys.Rev.* **C66** 034904 (2002) arXiv:nucl-ex/0206001v2

[71] [ALICE collaboration], *Phys.Lett.B* **708** (2012) DOI:10.1016/j.physletb.2012.01.060

[72] G. Gardim *et al.*, *Phys.Rev.* **C87** 031901(R) (2013) arXiv:1211.0989v2 [nucl-th]

[73] U.W. Heinz *et al.*, *Phys.Rev.* **C87** 034913 (2013) arXiv:1302.3535v2 [nucl-th]

[74] R.S. Bhalerao *et al. Phys.Lett.* **B580** 157-162 (2004) arXiv:nucl-th/0307018v2

[75] N. Borghini *et al. J.Phys.* **G30** S1213-S1216 (2004) arXiv:nucl-th/0402053

[76] S. A. Voloshin (2006) arXiv:nucl-th/0606022v2

[77] A. Bilandzic *et al.*, *Phys.Rev.* **C83** 044913 (2011) arXiv:1010.0233v2

[78] J. Qian *et al. Phys.Rev.* **C95** 054908 (2017) DOI:10.1103/PhysRevC.95.054908

[79] R.S. Bhalerao *et al.*, *Phys.Lett.B* **742** 94-98 (2015) arXiv:1411.5160v2

[80] [ALICE collaboration], The ALICE experiment at CERN LHC, *JINST* **3** (2008) S08002

[81] [ALICE collaboration], *J.Phys.G* **30** 1517 (2004)

[82] [ALICE collaboration], *J.Phys.G* **32** 1295 (2006)

[83] [ALICE collaboration], Performance of the ALICE VZERO system, *JINST* **8** (2013) P10016 arXiv:1306.3130v2 [nucl-ex]

[84] J. Qian *et al. Phys.Rev.* **C93** 064901 (2016) arXiv:1602.02813v2

[85] S. McDonald *et al.*, Hydrodynamic Predictions for Pb+Pb Collisions at 5.02 A TeV (2016) arXiv:1609.02958v3 [hep-ph]

[86] [ALICE collaboration], *Phys.Rev.Lett.* **107** 032301 (2011) arXiv:1105.3865 [nucl-ex]